Front. Phys., 2011, 6(2): 177–196
DOI 10.1007/s11467-011-0173-4

REVIEW ARTICLE

Advanced solar materials for thin-film photovoltaic cells

Fu-qiang HUANG[1,2,†], **Chong-yin YANG**[1,3], **Dong-yun WAN**[2]

[1] *College of Engineering and College of Chemistry and Molecular Engineering, Peking University, Beijing 100871, China*

[2] *CAS Key Laboratory of Materials for Energy Conversion, Shanghai Institute of Ceramics, Chinese Academy of Sciences, Shanghai 200050, China*

[3] *Suzhou Institute of Nano-Tech and Nano-Bionics, Chinese Academy of Sciences, Suzhou 215123, China*

E-mail: [†] *huangfq@pku.edu.cn*

Received November 21, 2010; accepted January 28, 2011

As one of the most promising solutions for the green energy, thin-film photovoltaic cell technology is still immature and far from large-scale industrialization. The major issue is getting low cost and stable module efficiency. To solve these problems, a large amount of advanced solar materials have been developed to improve all parts of solar cell modules. Here, some new solar material developments applied in different critical parts of chalcogenide thin-film photovoltaic cells are reviewed. The main efforts are focused on improving light trapping and antireflection, internal quantum efficiency and collection of photo-generated carriers.

Keywords thin-film solar cell, thin films, CIGS, CdTe

PACS numbers 73.40.Lq, 73.50.Gr, 84.60.Jt

Contents

1 Introduction

Over the last decades, energy crisis and environmental issues have continuously pushed the search for new renewable clean energy sources. The endlessness and zero carbon emissions of photovoltaic (PV) cells make them one of the most practical options. At present, the photovoltaic market is completely dominated by the products based on the use of silicon wafers, whose cost account for over 50% of the total module cost [1]. Since PV effect is based on series of surface and interface reactions, replacing wafers by thin-films of semiconductors deposited onto a supporting substrate – more commonly, a glass superstrate – is a great solution to reduce cost and improve efficiency.

The core of semiconductor solar cell is the p–n junction of the absorber layer, which converts photons into electron–hole pairs. The basic band diagram and working principle of a typical solar cell are shown in Fig. 1. The major absorber materials of solar cells (the p-doped semiconductors in Fig. 1) have optimal electronic structures to maximize the solar energy absorption. The whole process begins with the photons which have higher energies than the band gap transmitting their energies to crystal lattice. These energies are able to excite easily the localized valence electrons into the conduction band as free negative carriers. Meanwhile, the missing of the electrons in the valence band creates equivalent positive carriers called holes. Because of the Coulomb forces between them, these photo-generated electron–hole pairs will also be easily recombined in relaxation times. To prevent the recombination, the electric fields built by

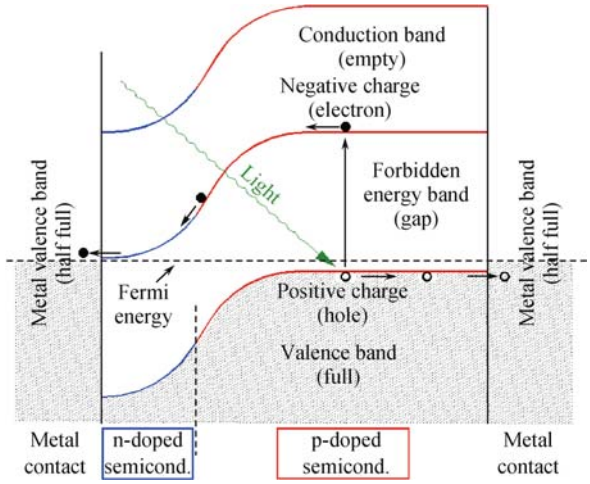

Fig. 1 Basic band diagram of a typical thin-film semiconductor solar cell.

potential difference of p–n junction interfaces effectively conduct electrons and holes to opposite directions. The contacts on the two sides collect all these electrons and holes into external circuits, which become the electrical energy to use. The typical J–V curves of solar cell devices shown in Fig. 2 behave just as the basic diode model, which can be described as the following equation,

$$J = J_0 \exp[q(V - R_s J)/(nkT)] + GV - J_L$$

where J_0, n, R_s, G are the saturation current density, the diode ideality factor, the series resistance and the shunt conductance, respectively. In the lift part of Fig. 2, the blue curve shows the dark current which is caused by the reversed diffusing of the carriers. The intercepts of the J–V curve on J-axis and V-axis are called the short circuit current (J_{SC}) and the open circuit voltage (V_{OC}), respectively. In the J–V curve, a particular point can give a maximum ($J \times V$) value. A very important parameter of solar cells called Fill Factor (FF) can be described as the following equation,

$$FF = \frac{\text{maximum } (J \times V)}{J_{SC} \times V_{OC}}$$

and the power efficiency η can be evaluated as the following equation,

$$\eta(\%) = \frac{FF \times V_{OC} \times J_{SC}}{\text{Sun light power}}$$

Nowadays thin-film technologies fall into two main classes; one based on silicon in amorphous, nanocrystalline and polycrystalline phases and another based on polycrystalline chalcogenide semiconducting compounds. Amorphous silicon (a-Si) solar cells have developed fast because of the mature semiconductor industry based on silicon. With about 10 at% hydrogen incorporated, the efficiency of a-Si/uc-Si hybrid solar cells has reached 12.5% (United Solar @ 2009), which is not high enough for application. However, a huge drawback of this solar cell is the light-induced degradation of material quality, which causes a big drop of the module efficiency after stabilizing.

The representatives of polycrystalline chalcogenide semiconducting compounds for PV cells are cadmium telluride (CdTe) and copper indium gallium selenide (CIGS). Device schematics for CdTe cell and CIGS cell are shown in Fig. 2. Two basic cells have similar layer structures, consisting of transparent conductive oxide (TCO) layer, n-type CdS buffer layer, p-type absorber layer and metal contact layer. The cost of CdTe solar cells are quite low and the efficiency has reached 16.7% (NREL @ 2001). The main issues with CdTe cells are the difficulties in p-type doping to CdTe and finding perfect back contact with right working function. The toxicity of cadmium is another issue that cannot be avoided. CIGS technology is a star performer in the laboratory with 20.3% efficiency demonstrated for small cells (ZSW @ 2010). The absorber layer of CIGS cell is very thin ($<$ 1 μm), which can save lots of raw materials. The chalcopyrite crystal structure provides many variables to optimize material performance. CIGS cell is one of the most promising thin film solar cells, which still has plenty of room for uptake. Meanwhile, a potential long-term issue with CIGS technology is the available resource of indium. Recently, a quaternary chalcogenide compound – copper zinc tin sulphide (CZTS) is considered as the next generation indium-free absorber materials, which might be the ideal substitute for CIGS.

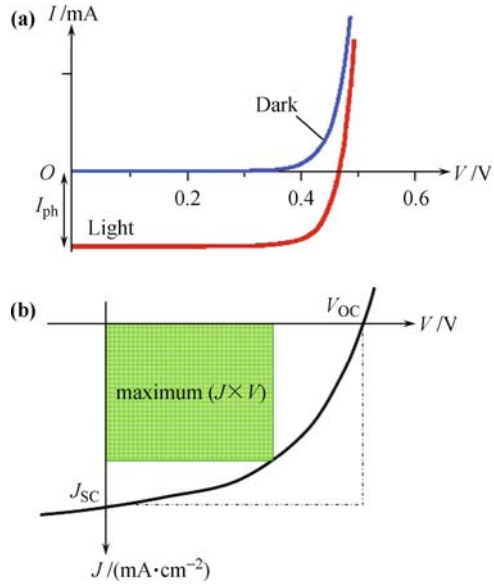

Fig. 2 Typical J–V curves of solar cells.

2 Advanced solar materials

Thin film solar cell modules are delicate and complicated systems, which have several function modules requiring unique solar materials to finish the whole solar energy

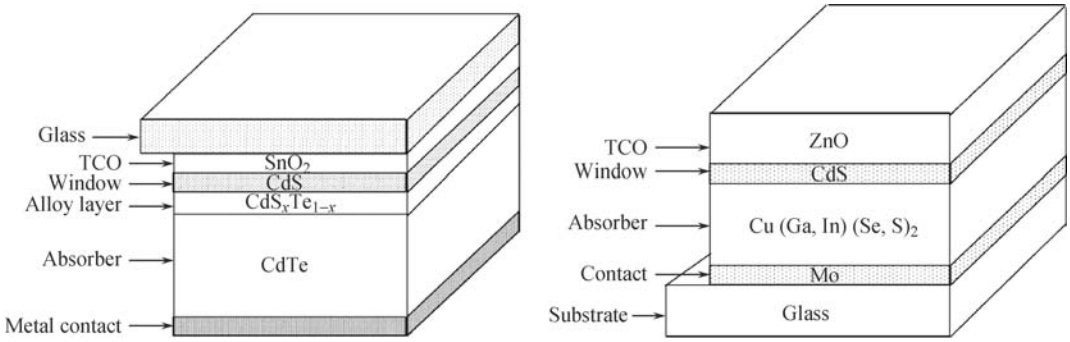

Fig. 3 Basic cell structures for CdTe cell (*left*) and CIGS cell (*right*).

conversion process. To improve the energy conversion efficiency of the entire devices, all kinds of advanced solar materials with higher performances are always worth pursuing. Figure 3 shows the basic scheme of different materials applied in thin film solar cell. The cores of these cell modules are p–n junctions formed by p-type and n-type photovoltaic semiconductors. In CdTe and CIGS cells, the major absorber materials are p-type polycrystalline semiconductors which should have optimized optical and electrical properties to absorb and convert photons. Meanwhile, n-type semiconductors should match the absorber materials forming built-in potentials to prevent electron–hole recombination and also be buffer layers to front contacts. Front and back contacts work as the collectors of photo-generated carriers and transfer them out. Hence, the contact materials should have high electron (or hole) conductivity and matched working functions to induce right current directions. Moreover, the front contact should be transparent windows to allow efficient light getting into the solar cell. To reduce the reflection of the surface, some antireflection materials can coat above the front contact. In this paper, several novel development of solar materials applied in different parts of chalcogenide thin film PV cells are reviewed.

2.1 Highly surface-textured ZnO:Al films for front contact

ZnO-based transparent conducting oxide (TCO) films, used as the front electrode in a-Si/μc-Si and CIGS thin-film solar cells, have attracted significant attention owing to low-cost and non-toxicity. A textured rough surface of the surface-textured ZnO films can improve the solar cell efficiency by allowing efficient light scattering inside the solar cell [2–6]. Recently, highly surface-textured ZnO:Al (AZO) thin films have been fabricated at room temperature in a two-step magnetron sputtering process using an oxygen-deficient ZnO target with small grain sizes [7]. The as-deposited AZO films are composed of a highly-oriented seed layer and a closely-packed columnar overlayer with pyramidal growth fronts, supporting a two-step mechanism of crystallite nucleation and grain growth. The structural, optical, and electrical properties of the AZO films can be tuned by the deposition conditions. The optimal two-step AZO film with the maximum RMS roughness of 40.2 nm reaches a very low square resistance of 0.66 Ω/sq ($\rho = 1.32 \times 10^{-4}$ Ω·cm) with an average transparency of 87.9% in the range of 400–1100 nm. The maximum haze factor of the as-deposited film is 60.7% at 360 nm, and the average haze is 14.8%. These properties are comparable to or exceed the reported values of surface-textured SnO_2-based and ZnO-based TCO films, making these films suitable for transparent electrode applications, especially in thin-film solar cells.

The as-prepared ZnO:Al (AZO) powders were obtained from the co-precipitation, and the AZO target was sintering from such powders with the addition of excess Zn. The SEM images of the as-prepared AZO powders and the ceramic AZO target are shown in Fig. 4. The density of the 850°C-sintered target is comparable with that of the commercial target sintered at 1300–1400°C, over 95% of the theoretical value, but our target has finer grains according to the SEM images presumably because of finer powders and the lower sintering temperature. The low-melting metallic Zn powders were used as the sintering agent during the low-temperature densification of the ceramic target. As a side effect of adding excess Zn, the resistance of the home-made AZO target reduced to less than 1.0 Ω/sq, lower than 3.0–7.0 Ω/sq

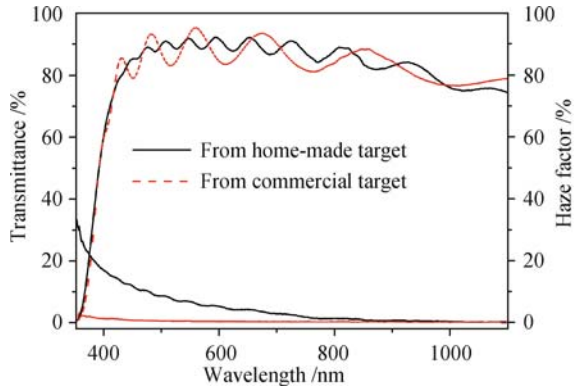

Fig. 4 Transmittance and haze spectra of one-step 100 W-deposited AZO films obtained from the home-made target (*solid lines*) and the commercial target (*dashed lines*).

of the commercial AZO targets with the same Al doping level.

The advantages of the home-made target are manifested in the property of the films made using (one-step) DC sputtering, typically at 100 W under 0.2 Pa Ar pressure for 30 min. A lower square resistance of 4.9 Ω/sq was observed for the films made from the home-made target, compared with 7.4 Ω/sq of the commercial one. The films have different morphologies as depicted by the SEM and AFM images in Fig. 5. The film obtained from the home-made target has a much rougher textured surface than that from the commercial one, in good agreement with the corresponding root mean square (RMS) roughness values of 14.2 nm and 5.34 nm. Their optical properties are also remarkably different, as shown in Fig. 4. Although the transmission is similar, the haze factor, which is the ratio of diffuse transmission to total transmission commonly used to indicate the light-capture ability of a surface-textured film, is much higher in the film made from the home-made target (28% at 360 nm vs. 2.3% at the same wavelength). Overall, the films from the home-made target also have superior electrical properties compared to those from the commercial one.

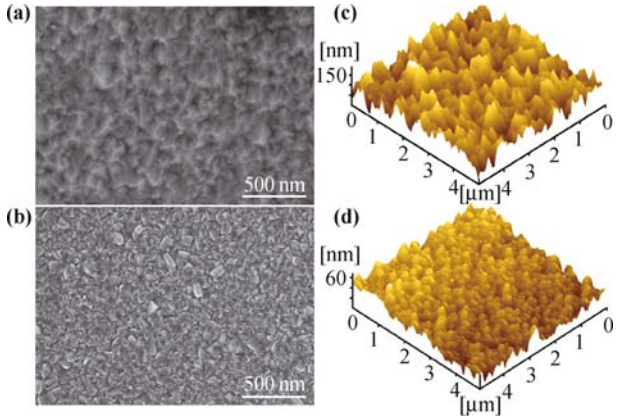

Fig. 5 SEM and AFM images of one-step 100W-deposited AZO films obtained from **(a**, **c)** the home-made target and **(b**, **d)** the commercial target. Reproduced from Ref. [7], Copyright © 2010 The American Chemistry Society.

The two-step deposition process was developed to promote seeding in the first layer, followed by textured growth in the overlayer. To aid crystal nucleation, a much lower power (60 W) together with a higher base pressure (1.2 Pa) were used in the first step to reduce the kinetic energy and the ion flux, which presumably could allow more time for surface diffusion and crystallization. The seed layer examined by SEM and TEM shows a thickness of about 200–300 nm. This highly-oriented and closely-packed seed layer provides an excellent substrate to grow a well-crystallized overlayer of the desired thickness. The overlayer was deposited at a higher power (80–140 W) and a lower pressure (0.2 Pa) to facilitate faster film growth without further nucleation of new grains. SEM and AFM images of the as-sputtered sample shown in Figs. 6 and 7 reveal well-crystallized AZO films with a rougher, more textured surface than those in Fig. 5. The corresponding average RMS roughness in a 3 μm× 3 μm area steadily increases from 15.1 to 40.2 nm with an increase of sputtering power from 80 to 140 W. The morphology and roughness of such a textured surface of the AZO films are comparable to those made from acid-etched sputtering (11) or LPCVD methods.

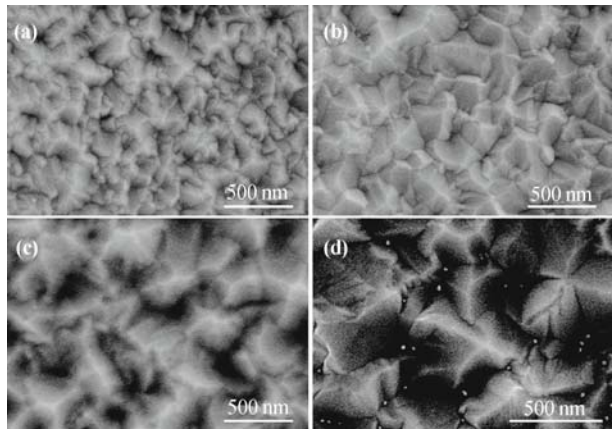

Fig. 6 SEM images of two-step sputtered AZO films deposited with different supplied powers: **(a)** 80 W, **(b)** 100 W, **(c)** 120 W, **(d)** 140 W, respectively. Reproduced from Ref. [7], Copyright © 2010 The American Chemistry Society.

During the two-step sputtering process, the growth of the overlayer and the surface texture is greatly influenced by the sputtering power. Under the same deposition condition of 100 W and 0.2 Pa, the two-step sputtering achieved much better-crystallized and rougher surface-textured films, which is as illustrated. The crystallinity of the as-deposited films can be indexed by peak intensity and full width at half maximum (FWHM) of the (002) diffraction peak. Since all the SEM images (Fig. 6) show a pyramidal microstructure on the surface, it is clear that the crystal growth of the overlayer proceeded by advancing faceted fronts around the [001] axis, which is also supported by the previous XRD and SAED patterns.

A microstructure comparison of the films obtained by two-step sputtering and one-step sputtering is seen in Fig. 8, showing cross-sectional SEM images of the two films. There is obvious columnar growth in the overlayer [Fig. 8(b)] in two-step sputtering, but even in one-step sputtering the growth eventually becomes columnar [Fig. 8(a)], which is schematically illustrated in the right side of Fig. 8 [8, 9]. However, as the power increases in the second step, the diameter of the columns increases (see Fig. 6), reaching 500 nm in Fig. 8(b) for 120 W. Such columnar growth with increasing diameters occurs because the faster growing grains tend to crowd out the slower growing grains when they all compete in the same growth direction. Since a higher power promotes faster growth in general, it also favors the selection of the fastest growing

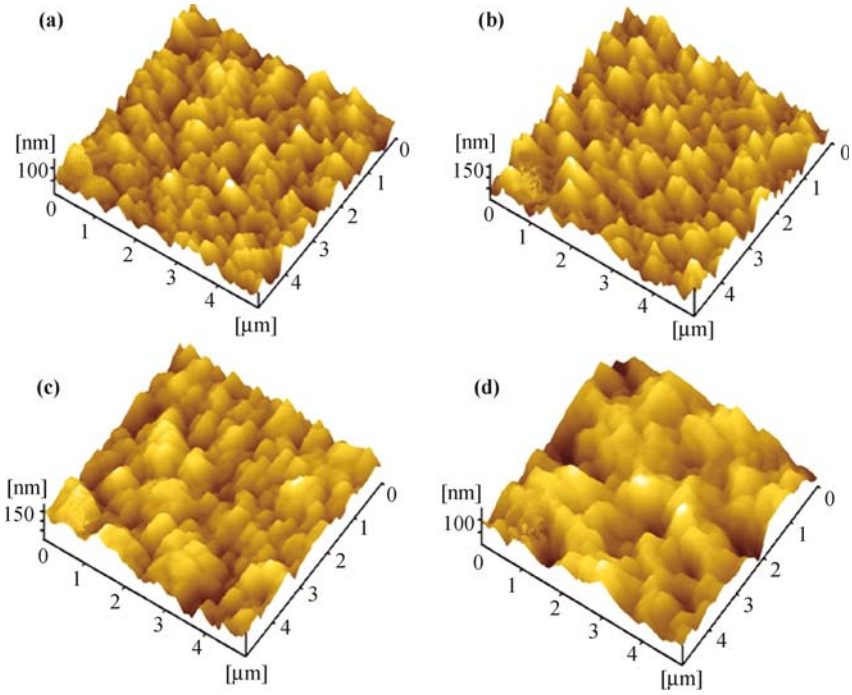

Fig. 7 AFM images of two-step sputtered AZO films deposited with different supplied powers, revealing the differences in grain size and morphology: **(a)** 80 W, **(b)** 100 W, **(c)** 120 W, and **(d)** 140 W, respectively. Reproduced from Ref. [7], Copyright © 2010 The American Chemistry Society.

grains. Therefore, the advantage of two-step sputtering lies in (i) nucleating a coat of smaller seed crystals that provide a more complete coverage of the substrate and more crystals to select for later fast growth; and (ii) faster growth conditions that favor fewer columns that grow to larger diameters while maintaining conformal coverage. As a result, a more coherent yet rougher surface-texture film takes shape.

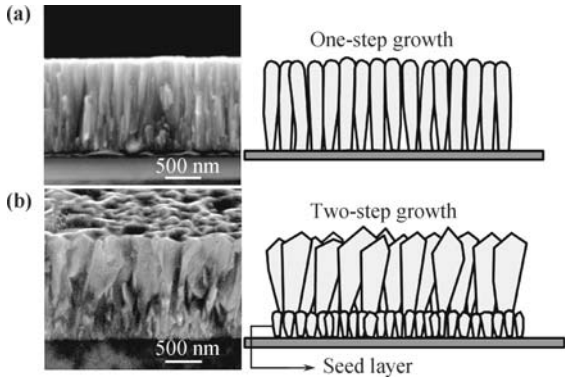

Fig. 8 SEM image of the cross section of **(a)** one-step 100 W-deposited AZO film, **(b)** two-step 120 W-deposited AZO film, the related schematic growth models of (a) one-step and (b) two-step AZO films are also shown. Reproduced from Ref. [7], Copyright © 2010 The American Chemistry Society.

As the sputtering power increases, the electrical resistivity and square resistance decrease from 5.16 Ω and 4.86×10^{-4} Ω·cm to 0.66 Ω and 1.32×10^{-4} Ω·cm, respectively, which may be attributed to the increasing grain size and better crystallization achieved at higher power. The correlation between mobility and sputtering power, however, is less clear. The mobility initially increases with the power, peaking at 120 W with the highest mobility of 35.4 $cm^2 \cdot V^{-1} \cdot s^{-1}$, then decreases somewhat at 140 W. The carrier concentration is relatively insensitive to the power, but all higher than 10^{21} cm^{-3}. These somewhat complicated correlations are not entirely surprising since mobility and conductivity in thin films are sensitive to not only crystal imperfection but also surface roughness, which increases with the sputtering power. The lowest resistivity of 1.32×10^{-4} Ω·cm achieved in the 140 W film is comparable to that of ITO films.

The optical properties of the two-step sputtered AZO films are shown in Fig. 9, which also includes other films in the literature for comparison. All the as-deposited samples show a very similar transmittance in the entire

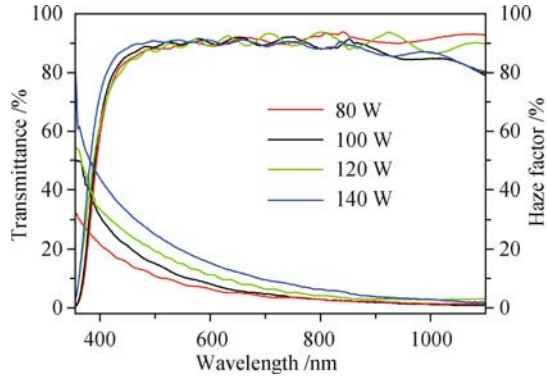

Fig. 9 Transmittance and haze spectra of two-step sputtered AZO films deposited with the four different supplied powers. Reproduced from Ref. [7], Copyright © 2010 The American Chemistry Society.

spectrum range in Fig. 9. The average transmittance in 400–800 nm is between 85% and 90% and remains very high for the near-infrared range. The 80 W film has a higher transmittance due to its thinner thickness. The higher transmittance of the 120 W film, especially in the near-infrared region, is consistent with its lowest carrier concentration which depresses the plasma frequency. Lastly, the haze factor increases with increasing power as expected from the rougher textured surface shown in Fig. 6.

The main purpose of this study is to develop a simple magnetron sputtering method at room temperature to fabricate surface-textured AZO films to manage the incoming light. For the 140 W-deposited AZO films, a high-quality textured surface was obtained with a maximum haze factor of 60.7% at 360 nm and the average haze of 14.8% in the range of 360–1100 nm. In contrast to our results, the typical Asahi-U with textured FTO films have the average haze factor of about 15%, the sheet resistance of 6 Ω/sq, and an resistivity of 8.59×10^{-4} Ω·cm, respectively [10]; The BZO films with the thickness of several microns are with an electrical resistivity of $\sim 10^{-3}$ Ω·cm, a haze factor of about 60% and the transmittance of about 80%. In summary, the low conductivity, high transmittance, and high haze factor of our films compare favorably with the best TCO films in the literature.

2.2 Molybdenum thin films for back contact of CIGS cells

Molybdenum (Mo) films have been selected as the best back ohmic contact for CIGS thin film solar cells, because it has a good chemical stability to resist not only the alloy of Cu, In, and Ga but also the gas of H_2Se or Se, and its working function well matches the absorber of CIGS [11, 12]. The magnetron sputtering depositions of molybdenum thin films, either by DC [5–15] or RF [16–24] techniques, have been widely studied during the fabrication of CIGS cells, but few comparative and systematic investigations were reported. To meet the requirements of back contacts of CIGS solar cells, RF and dc magnetron sputtering techniques have been applied to deposit Mo thin films at the different sputtering powers in the same system with the two-step process. Growth mechanisms of the Mo RF and DC-sputtered Mo films have been studied through the comparison of their structural, morphological, and electrical properties, respectively. The results first indicate that Mo films with similar structural and physical properties for CIGS solar cells use can be fabricated by the DC and RF techniques at the respective deposition conditions. Highly adhesive and conductive Mo films on soda lime glass have been optimized with the supplied power of 100 W of DC sputtering or 120 W of RF sputtering respectively. The optimized Mo films have been used as back contacts in thin film CIGS solar cells, and the as-fabricated solar cell reaches a high efficiency of 9.4%.

The FE-SEM images of the surface morphologies of the as-deposited Mo films are shown in Fig. 10. The surface texture of the Mo film increases with the increase of the supplied power, and the DC film has a much more textured surface than the RF film deposited at the same power value. The surface of the RF-80 W film is rather flat [Fig. 10(a)], but the fish-like texture can be observed for the DC-80 W film [Fig. 10(b)]. The surface textures in the RF-100 W and RF-120 W films are quite intense, but much more intense textures can be observed in the DC-100 W and DC-120 W films. The DC-100 W and RF-120 W films consist of large fish-like particles and similar grain sizes (∼70 nm), but the surface morphologies are something different, as shown in the FE-SEM images. The surface textures reflect the grain growth of these Mo films. The RF-80 W film consists of small grains (22.7 nm), and the DC-80 W film contains larger grains (37.5 nm).

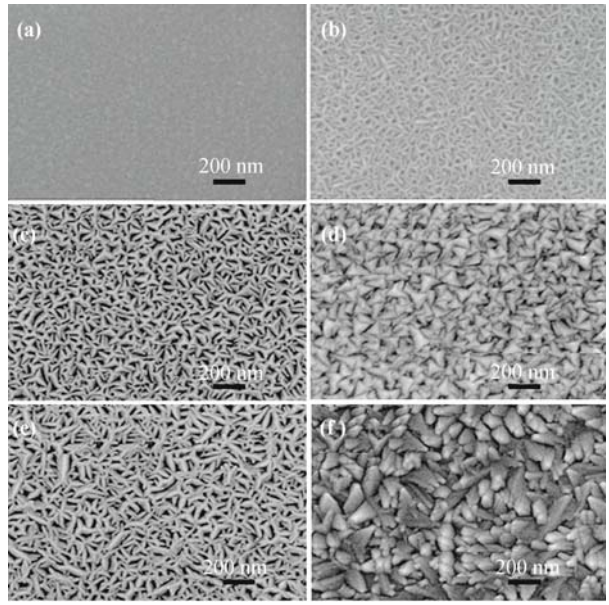

Fig. 10 SEM images of the Mo films prepared by DC and RF magnetron sputtering respectively with different supplied powers: **(a)** RF-80 W, **(b)** DC-80 W, **(c)** RF-100 W, **(d)** DC-100 W, **(e)** RF-120 W, **(f)** DC-120 W.

The textures can be evaluated from the roughness of the film surfaces, as the distinct AFM topographies are shown in Fig. 11. It can be seen that the AFM results are in good agreement with the SEM images. The RF-sputtered films show lower surface roughness than the respective DC-sputtered at the same supplied power value. For both RF and DC sputtering, the films deposited at higher power have rougher surface and larger grain size. The average RMS roughness of the RF-120 W film is 5.46 nm, but that of the DC-120 W film is up to 16.2 nm. Besides the grain size, this difference might be partially

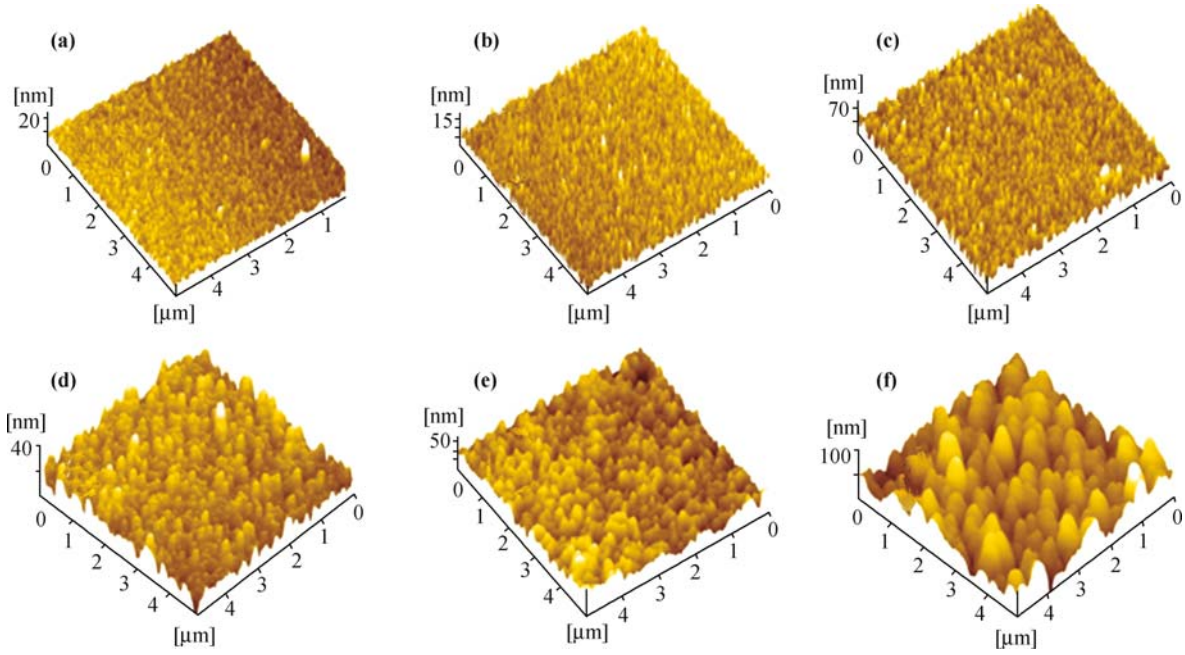

Fig. 11 AFM images of the Mo films prepared by DC and RF magnetron sputtering respectively with different supplied powers, revealing the differences in grain size and morphology: **(a)** RF-80 W, **(b)** DC-80 W, **(c)** RF-100 W, **(d)** DC-100 W, **(e)** RF-120 W, **(f)** DC-120 W.

attributed to the presence of larger voids and porous structure existing in the DC sputtering films [13]. The DC-100 W film has a similar average RMS roughness (4.96 nm) to the RF-120 W one (5.03 nm) with a concordant surface texture.

SEM observation of the cross-section for the DC and RF films are shown in Fig. 12. All the films consist of columnar grains, perpendicular to the substrate. Compared with the dc sputtered films, the RF sputtered films show a closer-packed microstructure. At the supply power of 100 W, both RF and DC sputtered films show a good adhesion between the Mo film and the soda-lime glass substrate. At the higher sputtering power of 120 W, a narrow gap is present in the interface for the dc sputtering, but the RF sputtered film still keeps well

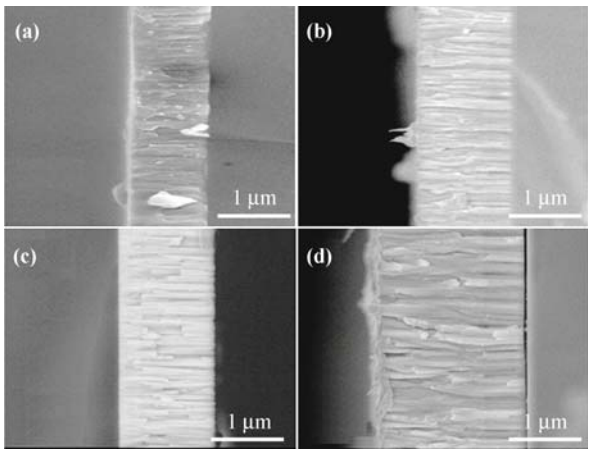

Fig. 12 Cross-sectional SEM images of the Mo films deposited at 100 W and 120 W by RF and DC sputtering respectively: **(a)** RF-100 W, **(b)** DC-100 W, **(c)** RF-120 W, **(d)** DC-120 W.

adhesive to the substrate. The DC-100 W and RF-120 W films both have a similar columnar cross section and a good adhesion between the Mo film and the soda-lime glass substrate.

It is customarily agreed that Mo films with adhesive properties depends strongly on the Ar pressure [14, 15]. According to the two-step deposition scheme, the first-step deposition at high pressure (2.4 Pa) serves as an intermediate adhesion between the substrate and the Mo film, and the second-step one at low pressure (0.6 Pa) grows the well-crystallized, highly conductive, and surface-textured overlayer. The high-pressure sputtering produce lower energy Mo atoms and lower deposition rate, and the initial Mo deposition as a buffer layer can reduce the stress between the film and the substrate.

On the other hand, the sputtering method and sputtering power also play great roles in the adhesive property. The DC sputtering process can generate larger grains and better-crystallized films than its counterpart RF sputtering. Meanwhile, the higher kinetic energy resulted from DC sputtering definitely reduce the buffering region and loosens the adhesion between Mo films and the substrate. Whereas, the RF sputtering reduces the energy of sputtered atoms and neutralized gas ions, which enable the less crystalline and smaller grains to gain better adhesion to the substrate, even with high power as 120 W. Also, it can be seen that the DC sputtering powers of 100 W and 120 W produce different adhesions to the substrates. In the high-power DC sputtering process of 120 W, the sputtered Mo atoms on the substrate have high energy, and the residue energy promotes the atom migration for further grain growth, then the charged Mo

atoms with higher energy form well-crystallized Mo films without the buffering adhesion to the substrate. From the cross-section images, DC sputtering allows for faster-growing films than RF sputtering at the same power value. The good adhesion between the Mo film and the soda-lime glass substrate for the DC-100 W and RF-120 W sputtered films might be attributed to their similar deposition rate and crystallization as mentioned above.

The resistivity of the Mo film highly depends on the sputtering method and the sputtering power. The electrical resistivity of the Mo film decreases with the increase of the supplied power, and the resistivity of the DC film is lower than that of the respective RF film. The DC-120 W film reaches the lowest resistivity of 1.02×10^{-5} Ω·cm and the lowest sheet resistance of 0.14 Ω. For the DC-100 W and RF-120 W sputtered films, both the samples reach a fairly low and similar resistivity and sheet resistance of 2.81×10^{-5} Ω·cm and 0.23 Ω, 2.78×10^{-5} Ω·cm and 0.24 Ω, respectively. The electrical resistance of the Mo film mainly results from grain boundaries. Distorted lattice, unsaturated bonds, and impurity segregation near the grain boundaries become the barriers for charge carriers to transport. The grain boundary barriers suppress carrier motion and decrease the conductivity of the film. The higher-power sputtered RF or DC film with larger grain size and better crystallization decreases the areas of the grain boundaries. As a result, the Mo films tend to have a lower conductivity.

As back contact electrode in CIGS solar cells, the desirable Mo film requires a low resistivity value of about $1 \times 10^{-5} - 5 \times 10^{-5}$ Ω·cm, which is achieved in the DC-100 W, DC-120 W, and RF-120 W sputtered films. Considering the good adhesion to the substrate, the DC-100 W and RF-120 W films qualify for the contact electrode of CIGS solar cells.

To examine the optimal Mo deposition condition, the Mo film prepared by the two-step DC sputtering at 100 W was used as the back contact of a CIGS solar cell. The Mo film served as not only the back contact of hole collector but also a good adhesive layer between glass and CIGS. The I–V characteristic of the fabricated 0.5×0.5 cm^2 CIGS solar cell is shown in Fig. 13(b). The photocurrent density of the cell is high up to 27.83 mA/cm^2 at AM1.5 illumination (100 mW/cm^2) at room temperature. The as-fabricated CIGS solar cell has an efficiency of 9.4% without an antireflective film. This result confirms that Mo film has well adhesive and highly conductive, and are very suitable for application as back contact electrodes of CIGS thin film solar cells.

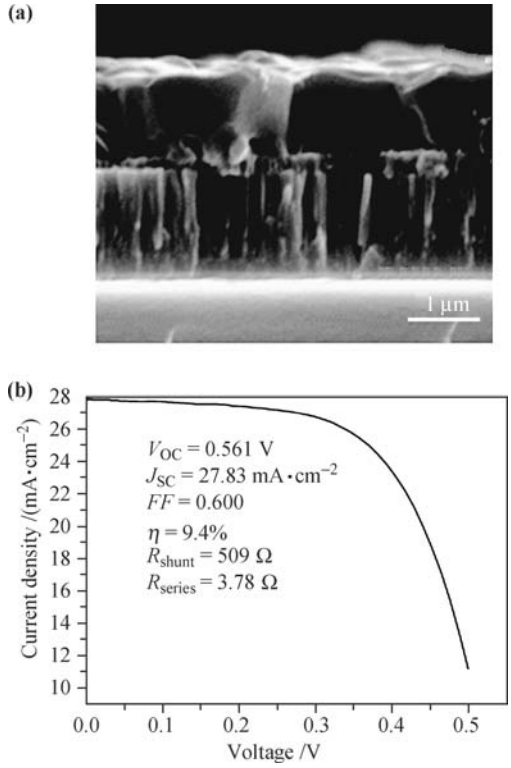

Fig. 13 **(a)** SEM cross-sectional image of the Glass/Mo/CIGS sample after selenization, **(b)** I–V characteristic of the CIGS solar cell.

2.3 Boron-doped graphene for back contact of CdTe cells

Graphene has recently attracted considerable attention owing to its excellent structural and electrical properties [14, 15]. As an electron-deficient system, boron doping can enhance the working function of graphene, which overcomes the lack of a suitable metal as an ohmic back contact for CdTe solar cells. A novel and versatile method has been explored to prepare freestanding pristine graphene (PG) and boron-doped graphene (BG). From the synthetic route, these graphene samples were formed rapidly from nascent carbon and boron in the reduction reactions of tetrachloromethane (CCl_4) and boron tribromide (BBr_3) by alkali metal potassium (K), respectively. The scanning electron microscopy (SEM) and transmission electron microscopy (TEM) images of the PG sample are displayed in Fig. 14. The architecture of sheets and the nanostructured carbon products are clearly demonstrated. Before sonication, the sample consists of flower-like nanosheets, as shown in the SEM image [Fig. 14(a)], and small stacked flakes are shown in the TEM images [Fig. 14(b) and (c)]. After sonication for 40 min in ethanol, single-layer graphene sheets with a topographic height of ∼0.7 nm were observed according to atomic force microscopy (AFM) characterization, as shown in Fig. 14(d), consistent with the reported single graphene [16, 17]. All the results indicate that the proposed method can conveniently synthesize single-layer graphene sheets. The morphology of boron-doped graphene is the same as pristine grapheme. These as-prepared graphene samples were used for further physical property measurements and device fabrications.

Boron doping introduces more holes in the valence

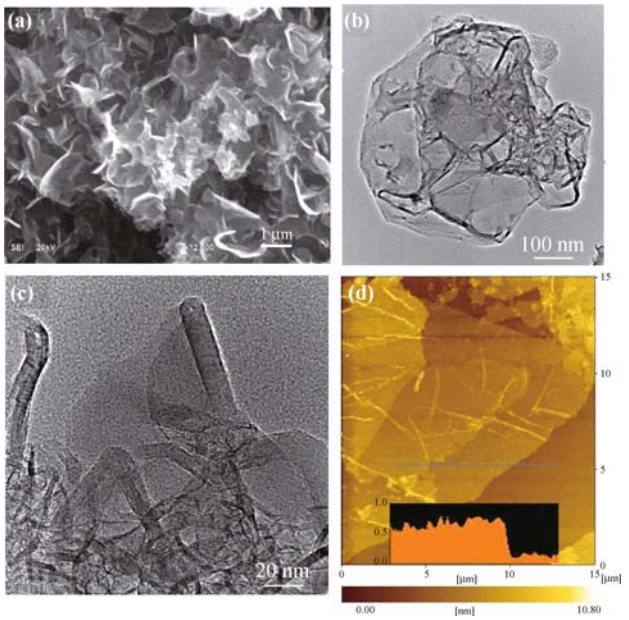

Fig. 14 **(a)** SEM, **(b)** and **(c)** TEM, and**(d)** AFM images of the pristine graphene (PG) sample. Reproduced from Ref. [16], Copyright © 2011 The Royal Society of Chemistry.

band of the graphene sheet, and larger carrier concentration of the sample is achieved. The electrical conductivities of CRG, PG, and BG were compared by the measurements of electrochemical impedance spectra (EIS). The CRG, PG and BG were fabricated to be film electrodes by blade coating method. As the Nyquist plots are shown in Fig. 15(a), the semicircle of PG is smaller than that of CRG, indicating that PG has much better conductivity than CRG. The result is consistent with the result of fewer defects in PG from Raman spectra. Especially in the boron-doped graphene, the charge-transfer impedance decreases dramatically, which means that the BG sample exhibits a higher electrical conductivity than PG owing to the increasing DOS value near Fermi level.

Conductive graphite paste is a good electrode (back contact) material to be served in CdTe solar cells. The working function of graphite nearly matches the CdTe absorber, and the highly polarized valence orbitals of Te (6s and 6p) have rather intense chemical interaction with the delocalized C $3p_z$ orbitals. In a CdTe solar cell, the CdTe absorber generates holes, which are injected into graphite electrode. Electrical conduction of graphite is anisotropic, and the hole conductivity (30–50 $S{\cdot}cm^{-1}$) perpendicular to the graphite layer is rather small compared with the inplane conductivity (10^6 $S{\cdot}cm^{-1}$) [18]. Strictly, the graphene sheet is a hexagonal carbon layer, and graphite is composed of many individual graphene layers packed along the c axis. For graphite, the interaction between graphene layers belongs to van der Waals force with slightly delocalized π–π^* interaction. Even the multilayer graphene with a perfect hexagonal carbon lattice can have smaller electrical resistivity along the c direction than the normal graphite. Reasonably, BG

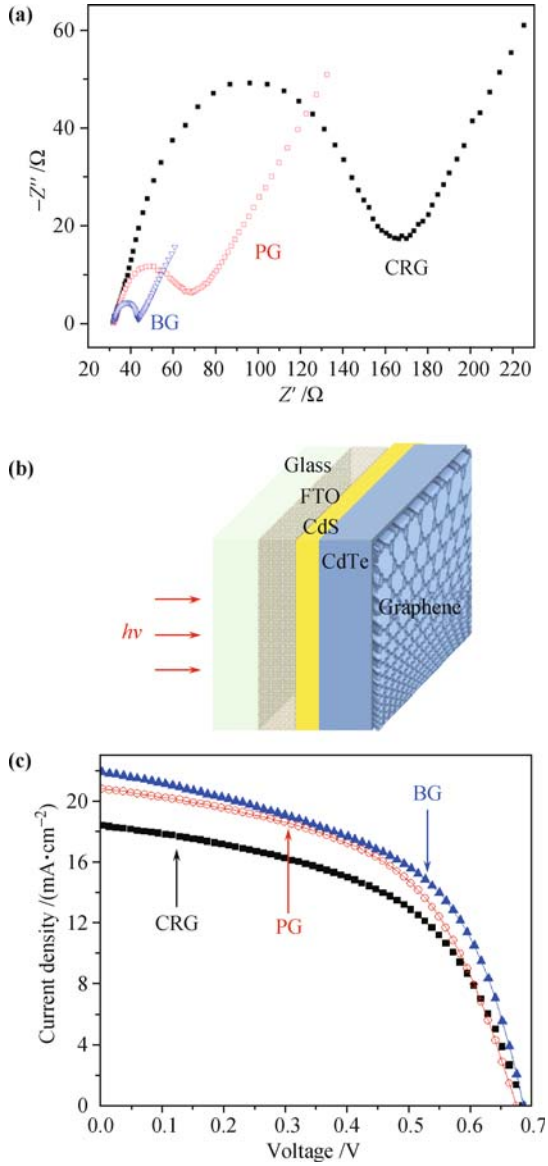

Fig. 15 **(a)** The typical electrochemical Nyquist plots of the CRG-modified, PG-modified and BG-modified electrodes, **(b)** the schematic CdTe solar cell with a graphene back electrode, and **(c)** I–V characteristics of CdTe solar cells with different back electrodes. Reproduced from Ref. [16], Copyright © 2011 The Royal Society of Chemistry.

sample is expected to act as better back electrodes of CdTe solar cells than PG, CRC, or regularly conductive carbon [Fig. 15(b)].

To further demonstrate the highly-conductive PG and BG to be back electrode materials of CdTe solar cells, the respective solar cells were fabricated, as shown in Fig. 15(b). The current–voltage (I–V) curves of the devices were measured, as shown in Fig. 15(c). The photovoltaic parameters are listed in Table 1. Based on the 1.0 cm^2 CdTe solar cell with the PG-based back electrode, a short-circuit photocurrent density (J_{SC}) of 20.81 $mA{\cdot}cm^{-2}$ with an open-circuit voltage (V_{OC}) of 0.674 V, calculated fill factor (FF) of 52.9%, and overall power conversion efficiency (η) of 7.41% have been obtained. The overall power conversion efficiency of the PG-based

cell is considerably higher than that of the CRG-based cell (6.50%), but lower than that of the BG-based cell (7.86%). The highly-conductive BG improved the hole-collected ability and reduce the barrier height to enhance the overall power conversion efficiency. The J_{SC} value of the BG-based cell is 21.96 mA·cm^{-2}, and those of the CRG and PG-based cells are 18.38 and 20.81 mA·cm^{-2}, respectively. The improved overall power conversion efficiency of the BG-based cell is attributed to that the boron doping can improve the working function of graphene and form a good ohmic contact with the p-CdTe.

Table 1 Photovoltaic performance of CRG-, PG-, and BG-based CdTe solar cells.

Back electrode	J_{SC} /(mA· cm^{-2})	V_{OC} /V	FF /%	η /%
CRG	18.38	0.685	51.6	6.50
PG	20.81	0.674	52.9	7.41
BG	21.96	0.685	52.2	7.86

Note: Reproduced from Ref. [16], Copyright © 2011 The Royal Society of Chemistry.

2.4 Nanostructured ZnO/SiO_2 for broadband antireflection coatings

Antireflective coatings (ARCs) have been widely used to increase the solar radiation absorption in solar collectors such as solar cells, and to reduce front surface reflection of selective absorbers [19] as well as collector glass covers [20–24]. Novel schematic refractive-index-gradient coatings of nanostructured ZnO/SiO_2 were proposed to possess a broadband antireflection over the solar spectrum. Such double-layer coatings were successfully prepared on the surface of glass substrates via sol-gel dip-coating process. Sol-gel process comes out as a versatile method with its high process speed, low-cost, suitability for continuous production and essentially forming porous nanostructure with adjustable refractive index by precise control on the pore volume, pore size and surface area [25]. The broadband performance of the double-layer antireflective structure is achieved, and a wide and flat antireflection band ranging from 475 nm to 900 nm appears. The average transmittance is increased by 6.90%, and the near infrared transmittance is increased by 6.04%. The improvement of transmittance contributes to the destructive interference in light reflected from interfaces between the different refractive-index layers with an optimized thickness. Such novel antireflective coatings of ZnO/SiO_2 provide a promising route for solar energy applications.

The surface and cross-section morphologies of the ZnO, SiO_2 and ZnO/SiO_2 coatings were investigated by FE-SEM and TEM, as shown in Fig. 16(a)–(d). The surface morphology of ZnO coating consists of agglomerated ZnO nanoparticles and some cracks [Fig. 16(a)]. The ZnO grains with a size of about 30 nm are much smaller than the wavelength of visible light, which implies that Mie and Rayleigh scattering can be neglected. The ZnO single layer can be treated as a single homogeneous coating with a uniform refractive index in the visible light region. Figure 16(b) shows the TEM image, and the inset gives

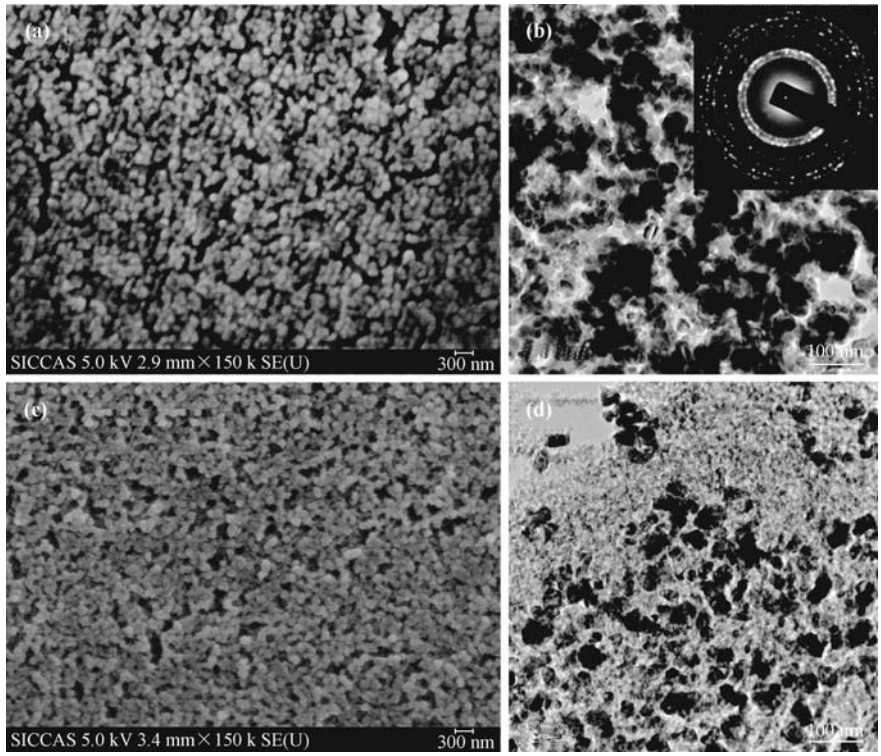

Fig. 16 SEM **(a)** and TEM **(b)** images of the ZnO coating (inset: electron diffraction pattern), and SEM **(c)** and TEM **(d)** images of the ZnO/SiO_2 coating.

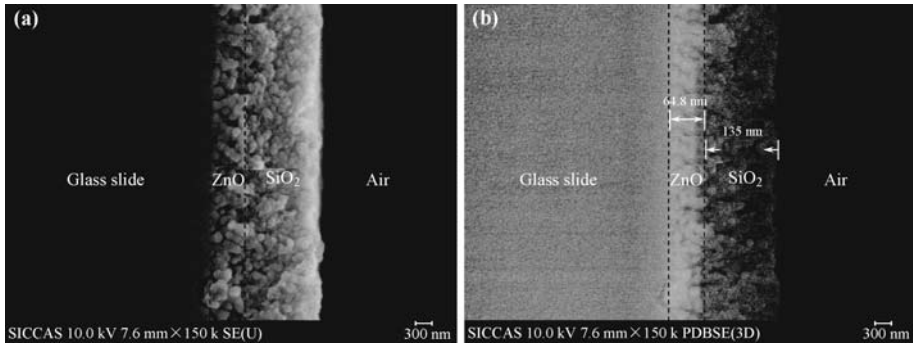

Fig. 17 Field emission SEM **(a)** and backscattered electron **(b)** images of cross-sectional ZnO/SiO_2 coating.

the corresponding selected-area electron diffraction pattern of the ZnO coating. As shown in the inset, the ZnO coating is polycrystalline and mainly hexagonal wurtzite ZnO structure, which agrees with the XRD results well.

The surface morphology of the ZnO/SiO_2 double-layer coating is shown in Fig. 16(c). The toplayer is a porous SiO_2 layer consisting of particle clusters and pores with the sizes about 20 nm and 40 nm, respectively. In the TEM image of the ZnO/SiO_2 coating [Fig. 16(d)], the two-layer microstructure is observed, which is composed of black particles corresponding to ZnO layer, and the light-color region referring to amorphous SiO_2 layer.

The detailed structure of the double-layer coating was further analyzed using FE-SEM and backscattered electron images (BEI) of FE-SEM. The cross-sectional morphology of the coating on the glass slide substrate was shown in Fig. 17(a). The coating contains the two layers of the top SiO_2 (smaller particles) and the bottom ZnO (larger particles). The interfaces of substrate/ZnO, SiO_2/air and ZnO/SiO_2 are clearly observed, as are indicated with the black dash lines in the figure. BEI was used to detect contrast between areas with different chemical compositions. Backscattered electrons of heavy element (Zn) are stronger than light element (Si), and thus appear brighter in the image. The brighter bottom layer is ZnO, and the top layer is SiO_2 [Fig. 17(b)]. From FE-SEM and BEI images, the thicknesses of the SiO_2 and ZnO layers are approximately determined to be 135 $\pm$ 5 nm and 65 $\pm$ 5 nm, respectively.

Intrinsic bulk ZnO is a wide-band-gap semiconductor (3.2 eV), and bulk SiO_2 is a typical insulator. Both materials have a direct transition band gap. E_g values of ZnO and SiO_2 layers are found to be 3.27 eV and 4.15 eV, respectively. The wide optical band gaps of ZnO and SiO_2, larger than the energy of visible light, indicate that these materials are suitable for applications of ARCs. The dependence of optical constants such as refractive index (n) and extinction coefficient (k) of ZnO and SiO_2 single layer on wavelengths were determined by ellipsometer. The dispersion plays an important role in design and research of ARCs. Double-layer coating was designed with refractive-index-gradient structures, and n of ZnO and SiO_2 are 1.34 and 1.21 at 550 nm, respectively. In the visible-light region, k value of ZnO is less than 0.16, and that of SiO_2 is less than 0.0005, which indicates that the weak absorption of the sol-gel deposited coatings is suitable for the ARCs of solar glass.

Transmittance spectra of ZnO/SiO_2 double-layer samples are over the wide range of the solar spectrum, as shown in Fig. 18. The respective average transmittances of ZnO single layer in the visible and NIR light regions are increased by 3.32% and 2.48% (SiO_2: 5.23% and 3.17%), compared with the blank glass slide. The maximum transmittances appear at about 550 nm. The transmittance improvement observed in either ZnO or SiO_2 single layer can cover only a very narrow bandwidth in the entire solar spectrum.

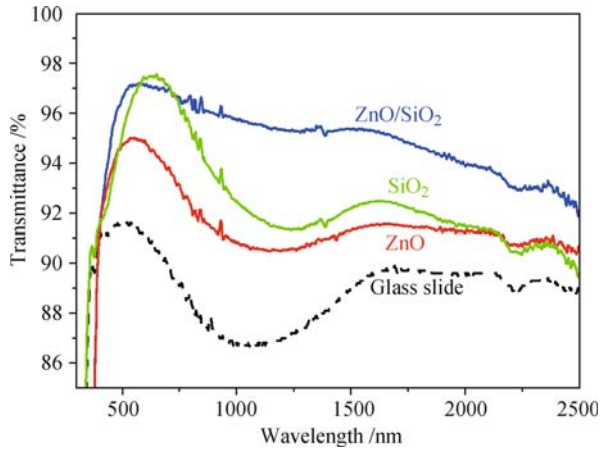

Fig. 18 Comparative transmittance spectra of blank glass slide and those coated with ZnO, SiO_2, and ZnO/SiO_2.

The average transmittance of the ZnO/SiO_2 double-layer structure in visible region is 96.31%, increased by 5.72%. There is a very wide and relatively flat antireflective band ranging from 475 nm to 900 nm and the average transmittance is 96.7%, increased by 6.90%, which will greatly reduce energy loss and improve efficiency for solar cell applications. The transmittance improvement of the double-layer structure in NIR region is particularly important to achieving a broadband transmittance. The average transmittance of the double layer is increased by 6.04%, much higher than 3.17% and 2.48% in the SiO_2

and ZnO single layers, respectively. The approximate distribution of solar energy is 7% in ultraviolet region, 50% in visible region and 43% in NIR region. Compared with the transmittance improvement of SiO_2 single-layer coating, the ZnO/SiO_2 double-layer ARCs reveal the superiority and importance in collecting solar energy, especially in NIR region for photovoltaic and thermoelectric solar energy conversions. The glass slide substrate has a transmittance of 89.0% in the range of 400–2500 nm, and the losses of light reflection and absorption are 7%–9% and 2%–4%, respectively. The peak at 360 nm is due to the absorption of glass substrate, and the intrinsic band gap of the ZnO semiconductor (3.27 eV) is at 380 nm. The average reflectance of ZnO/SiO_2 double-layer structure in 400–2500 nm and NIR region is 3.16% and 3.23%, respectively (6.58% and 6.73% for ZnO; 3.74% and 4.0% for SiO_2).

The suppression of the reflection by ZnO/SiO_2 double-layer is improved over the solar spectrum, compared with the reflectance of SiO_2 single layer which increases quickly far from the minimum. The antireflective performance is also verified from the photograph of our sample, as shown in Fig. 19. The blank part of glass substrate has more intense light reflection than the ZnO/SiO_2-coated (ARC) part. No obvious light scattering is found in the ARC part, revealing a high quality in appearance. For this gradient index stack, the overall reflectance is affected by two key parameters: (i) the index discontinuity at each interface including the interfaces of the stack with the substrate and with the ambient air, and (ii) the total thickness of the stack which affects the free spectral range. The antireflective performance can be further enhanced via modification of the ARC synthesis and optimization of the nanostructure design.

Fig. 19 Photograph of the glass slide substrate half-coated with ZnO/SiO_2.

2.5 $Cd_{1-x}Zn_xS$ thin films for the buffer layer

Cadmium sulfide (CdS), an n-type semiconductor with a direct transition band gap of 2.4 eV, has been found to be the best buffer layer for CIGS solar cells. However, the quantum efficiency of CIGS/CdS solar cells drops at the short wavelength range (<520 nm) due to the optical absorption loss of CdS. As a perfect candidate, the $Cd_{1-x}Zn_xS$ thin film has gained prominence for its tunable wide band gap from 2.4 eV ($x = 0$) to 3.8 eV ($x = 1$) [26]. The comprehensive optical characterization of $Cd_{1-x}Zn_xS$ thin films is required for further investigation and understanding. The photovoltaic $Cd_{1-x}Zn_xS$ thin films, fabricated by chemical bath deposition, have been successfully used as n-type buffer layer in $CuInGaSe_2$ (CIGS) solar cells [27]. Comprehensive optical properties of the $Cd_{1-x}Zn_xS$ thin films were measured and modeled by spectroscopic ellipsometry (SE), which is proven to be an excellent and non-destructive technique to determine optical properties of thin films. The optical band-gap of $Cd_{1-x}Zn_xS$ thin films can be tuned from 2.43 eV to 3.25 eV by controlling the Zn content (x) and deposition conditions. The wider-band-gap $Cd_{1-x}Zn_xS$ film was found to be favorable to improving the quantum efficiency in the wavelength range of 450–550 nm, resulting in an increase of short-circuits current for solar cells. From the characterization of quantum efficiency (QE) and current–voltage curve (J–V) of CIGS cells, the $Cd_{1-x}Zn_xS$ films ($x = 0.32$, 0.45) were demonstrated to significantly enhance the photovoltaic performance of CIGS solar cell. The highest efficiency (10.5%) of CIGS solar cell was obtained using a dense and homogenous $Cd_{0.68}Zn_{0.32}S$ thin film as the buffer layer.

Plots of ellipsometric spectra of the experimental ellipsometric angles $\Psi(\lambda)$ and $\delta(\lambda)$ for the $Cd_{1-x}Zn_xS$ films on the ITO substrates were shown in Fig. 20, respectively. The experimental data were analyzed by using a four-layer model of glass/ITO/$Cd_{1-x}Zn_xS$/air, where $Cd_{1-x}Zn_xS$ is a mixture layer consisting of the interface of ITO and $Cd_{1-x}Zn_xS$, the as-deposited $Cd_{1-x}Zn_xS$ film, and the rough surface of $Cd_{1-x}Zn_xS$. The Cauchy fitting was used to pre-estimate and generate an initial value for the following Lorentz fitting. An accurate determination of the film thickness and optical constants was achieved by modeling the material with one or more Lorentz Oscillators. The variables, the optical parameters (n, k) and the layer thickness (d) of thin film, were optimized by using a modified Levenberg–Marquardt algorithm to minimize the root mean square error (RMSE)

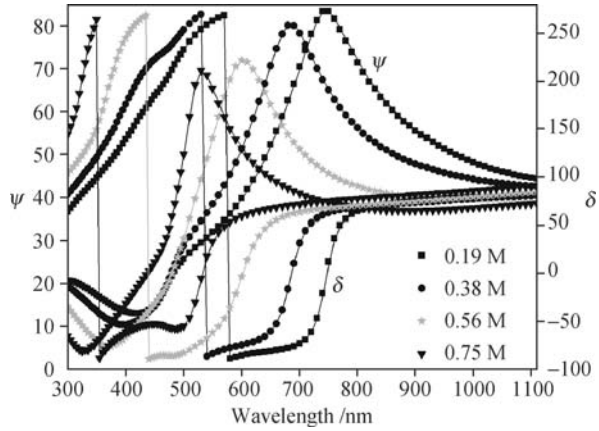

Fig. 20 Ellipsometric $\Psi(\lambda)$ and $\delta(\lambda)$ spectra of $Cd_{1-x}Zn_xS$ thin films deposited at different ammonia concentrations. The solid lines represent the best fit from the theoretical model.

between the experimental and fitted ellipsometric angles ($\Psi(\lambda)$, $\delta(\lambda)$). The optical constants (n, k) of thin film were described by a dispersion relation [28], and the surface roughness of the mixture layer and the Zn content (x) in the film were both determined by the fit. The fitted and experimental data were in a good agreement when RMSE is between 0 and 1. The refraction indices were obtained by fitting measured ellipsometric data. From the optical constants, dielectric function $\varepsilon(\varepsilon_1 + \mathrm{i}\varepsilon_2) = (n + \mathrm{i}k)^2$ and absorption coefficients ($\alpha = 4k\pi/\lambda$) of the films were calculated as a function of wavelength (λ).

At ammonia concentration equal to 0.19 M, there was no sufficient NH_3 to bind Cd^{2+} and Zn^{2+} forming tetraamine complexes. This led to an excess of Cd^{2+}, Zn^{2+} and S^{2-} in the deposition bath and the homogenous nucleation of $Cd_{1-x}Zn_xS$ colloids in solution with weak film adhesion. This process was dominated by the first growth stage for CBD $Cd_{1-x}Zn_xS$ deposition [29] (homogeneous reaction process). Simultaneously, other heterogeneous reactions took place, and many nucleation sites of $Zn(OH)_2$ and ZnO were deposited on the substrate. The film containing colloidal particles was not packed compactly, the surface roughness (44.5 nm) was large, and E_g was 3.25 eV due to high Zn content.

As ammonia concentration increased, the heterogeneous reactions dominated the growth stage for CBD $Cd_{1-x}Zn_xS$ deposition. This concentration was high enough for Zn^{2+} and Cd^{2+} to form tetraamine metal complex ions, which was used to control the reaction rate and to prevent the immediate precipitation in the solution. Furthermore, ammonia hydrolysis provided the alkaline condition. [OH^-] was adequate to initiate the hydrolysis of $SC(NH_2)_2$ on the substrate, but still low to generate small amount of S^{2-}. Otherwise, this reaction would be homogeneous. The thin film deposited through atom-by-atom was very compact and excellently adherent to the substrate. The film thickness increased and the surface roughness decreased.

As ammonia concentration further increased, the thickness and roughness of thin films both decreased. High ammonia concentration stabilized tetraamine complexes to reduce the growth rate. This low growth rate prevented the progression of the reaction into the next stage, cluster-by-cluster process in a short time. Moreover, high ammonia concentration generated more OH^- in reaction bath, leading to excess amount of S^{2-} and the formation of $Cd_{1-x}Zn_xS$ colloids in solution. CdS deposition was to less extent on the substrates because the solubility product of CdS ($K_{sp} = 10^{-28}$) was far lower than CBD-ZnS ($K_{sp} = 3 \times 10^{-25}$). Therefore, the Zn content in thin films decreased with the increase of ammonia concentration.

The absorption coefficient (α) of $Cd_{1-x}Zn_xS$ thin films were calculated as a function of wavelength by the relationship with extinction coefficient [$\alpha = (4k\pi)/\lambda$]. The band gap (E_g) was calculated from the equation of $\alpha h\nu = K(h\nu - E_g)^{n/2}$ [30], where $h\nu$ is photon energy, n and K are constants, and n is equal to 1 for direct-band-gap semiconductors ($Cd_{1-x}Zn_xS$). The value of E_g was determined by extrapolating the linear portion of the plots of $(\alpha h\nu)^2$ versus $h\nu$ to $\alpha = 0$ on the $h\nu$ axis. The plots of $(\alpha h\nu)^2$ versus $h\nu$ for the $Cd_{1-x}Zn_xS$ thin films were shown in Fig. 21. The E_g value of the $Cd_{1-x}Zn_xS$ film depends on the Zn content x and the film thickness. The $Cd_{1-x}Zn_xS$ thin film, deposited at 0.19 M ammonia, had $x \approx 0.90$ and $E_g \approx 3.25$ eV. Its broader absorption edge implies that the as-prepared film is not phase-pure, in good agreement with XRD results (not shown here). However, the sharp absorption edges of other $Cd_{1-x}Zn_xS$ films at the different ammonia concentrations were characteristic of homogeneous phases. Their E_g values of 2.43 eV, 2.45eV, and 2.52 eV were related with the Zn content and film thickness. Therefore, the quality of $Cd_{1-x}Zn_xS$ films can be estimated from their optical properties.

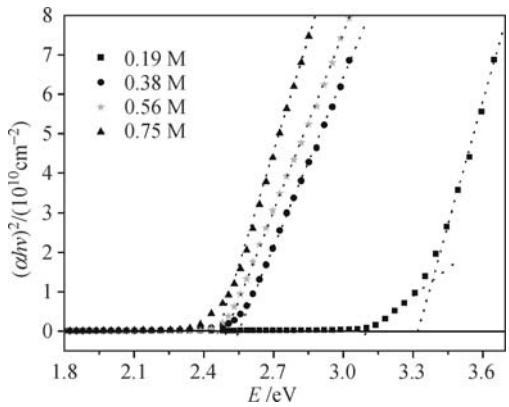

Fig. 21 Plots of $(\alpha h\nu)^2$ versus photon energy $h\nu$ for $Cd_{1-x}Zn_xS$ thin films at different ammonia concentration.

CIGS cells with different $Cd_{1-x}Zn_xS$ thin films as the buffer layer were characterized by quantum efficiency (QE) and illuminated current–voltage density (J–V), as shown in Figs. 22 and 23. The dropping edge in QE of solar cells shifted toward the blue light region with lower k above E_g, which indicated that more light passed through the buffer layer and was absorbed by the CIGS layer. As shown in Fig. 23, the increase of Zn content in $Cd_{1-x}Zn_xS$ caused the increase of short-circuit current (J_{SC}) while the open-circuit voltage (V_{OC}) decreased. After the systemic study of $Cd_{1-x}Zn_xS$ thin films, excessive Zn content would result in bad optical properties, and deteriorate the device performance. The fact was evident by comparing the buffer layer $Cd_{1-x}Zn_xS$ thin films at 0.19 M and 0.56 M ammonia. The former one had abnormally low refractive index, broad absorption edge, non-uniform phase and high surface roughness, which caused the lowest solar cell efficiency (8.9%). Therefore, optimization of $Cd_{1-x}Zn_xS$ thin film optical properties was essential for the improvement of solar cell performance. The buffer layer $Cd_{1-x}Zn_xS$ with refractive index between 2.0 and

2.4, extinction coefficient increasing slowly above band gap (Fig. 20), and corresponding sharp absorption edge (Fig. 21) could jointly guarantee higher solar cell efficiency.

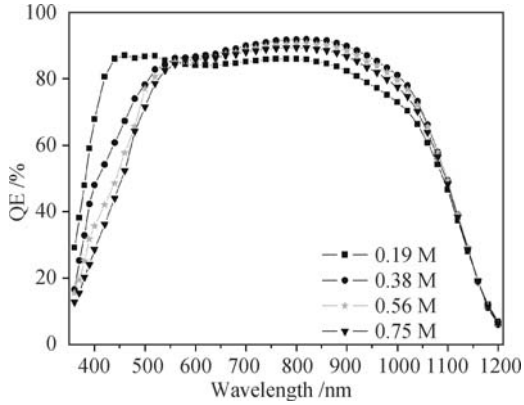

Fig. 22 Quantum efficiency (QE) characteristics of CIGS solar cells with $Cd_{1-x}Zn_xS$ window layer under different ammonia concentration.

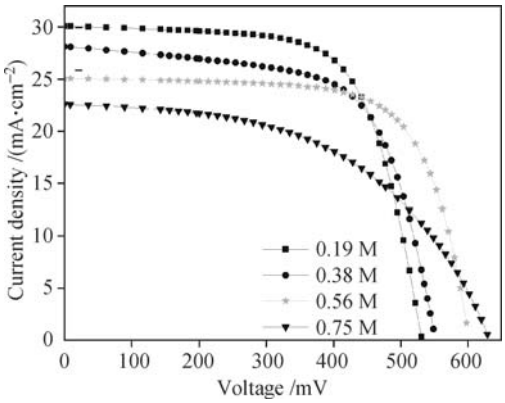

Fig. 23 *J–V* characteristics of CIGS solar cells with $Cd_{1-x}Zn_xS$ window layer under different ammonia concentration.

2.6 Fundamental researches of $CuInSe_2$ for the absorber layer

As one of the most promising semiconductor materials used in solar cells, $CuInSe_2$ attracts great attentions for its synthesis kinetics, physical and chemical properties [30, 31]. To achieve high quality CIGS films, fundamental researches to fully investigate $CuInSe_2$ compound are quite necessary [32–36]. Many studies have shown that the energy conversion efficiency can be improved by doping [37–39]. Bulk samples of $Cu_{1+x}In_{1-x}Se_2$ (x = 0–0.5) have been prepared by solid-state reaction method at 1073 K. The structure, thermal stability, optical and electrical properties were systematically studied. For the sample of $Cu_{1+x}In_{1-x}Se_2$ with x increasing from 0 to 0.5, the optical band gap of is gradually reduced from 0.9 eV to 0.86 eV. Moreover, the room temperature electrical conductivity has been greatly enhanced from 5 S/cm to 850 S/cm, and Seebeck coefficient is slightly decreased from 35 μV/K to 25 μV/K. It is likely that lattice distortions and additional holes introduced by Cu doping are attributed to the improved conductivity and the decreased band gap and Seebeck coefficient.

Figure 24 presents the TG curves for $Cu_{1+x}In_{1-x}Se_2$ (x = 0–0.5) samples within the temperature range of 300–800 K at a heating rate of 5 K/min. Almost no weight loss appears below 625 K for all the samples. But some weight loss occurs above 625 K, and the weight loss ranges from 0.9 wt% to 1.9 wt% along with the increase of x at 800 K. The inset displays that the weight loss at 800 K depends linearly on x. This feature may be resulted from the instability of Cu^{2+}-containing selenides at high temperature without the protection of selenium atmosphere due to the reduction of Cu^{2+} into Cu^{+}, and thus the excessive Se was released [40]. Overall, $Cu_{1+x}In_{1-x}Se_2$ (x = 0–0.5) is thermally stable up to 625 K, comparable to the working temperature of currently available solar cells.

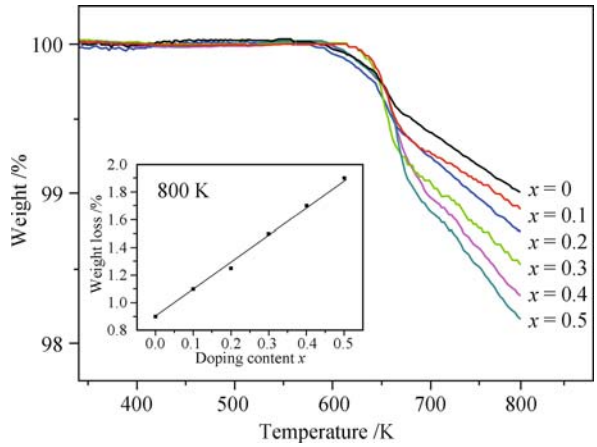

Fig. 24 TG curves for $Cu_{1+x}In_{1-x}Se_2$ (x = 0–0.5) samples. The insert shows the weight loss as a function of Cu doping content x at 800 K.

UV/Vis/NIR diffuse reflectance measurements were performed on the powder samples of $Cu_{1+x}In_{1-x}Se_2$ (x = 0–0.5), as shown in Fig. 25. The optical band gaps of $Cu_{1+x}In_{1-x}Se_2$ (x = 0.0, 0.2, 0.4, 0.5) are 0.9, 0.89, 0.87, and 0.86 eV, respectively. The band gap of

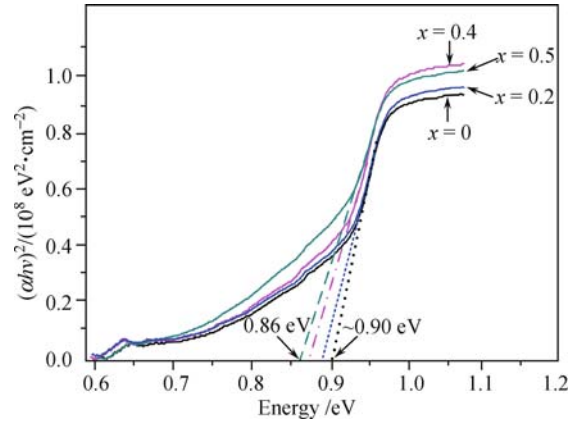

Fig. 25 The plots of $(\alpha h\nu)^2$ versus photo energy for $Cu_{1+x}In_{1-x}Se_2$ (x = 0–0.5) samples.

$Cu_{1+x}In_{1-x}Se_2$ ($x = 0$–0.5) decreased gradually with the increase of Cu-doping concentration. It might result from the valence band maximum (VBM) caused by stronger hybridation of Cu 3d and Se 4p obitals with the increase of Cu-doping concentration [41].

Since $Cu_{1+x}In_{1-x}Se_2$ ($x = 0$–0.5) is stable only below 625 K, the electrical conductivity and Seebeck coefficient measurements were scanned from room temperature to around 625 K. The temperature dependence of electrical conductivity of $Cu_{1+x}In_{1-x}Se_2$ ($x = 0$–0.5) is shown in Fig. 26. The electrical conductivities of the blank $CuInSe_2$ sample can be greatly improved by the substitution of In by Cu at room temperature from 8 S/cm ($CuInSe_2$) to 440 S/cm ($Cu_{1.4}In_{0.4}Se_2$) and 850 S/cm ($Cu_{1.5}In_{0.5}Se_2$). At 625 K, the electrical conductivity is only 5 S/cm for the blank $CuInSe_2$, but 320 S/cm for the $Cu_{1.4}In_{0.6}Se_2$ and 400 S/cm for $Cu_{1.5}In_{0.5}Se_2$. In addition, a sharp increase in electrical conductivity was observed when x increased from 0.3 to 0.4, which can be ascribed to the appearance of a highly conductive second phase CuSe [42], as is consistent with the XRD results.

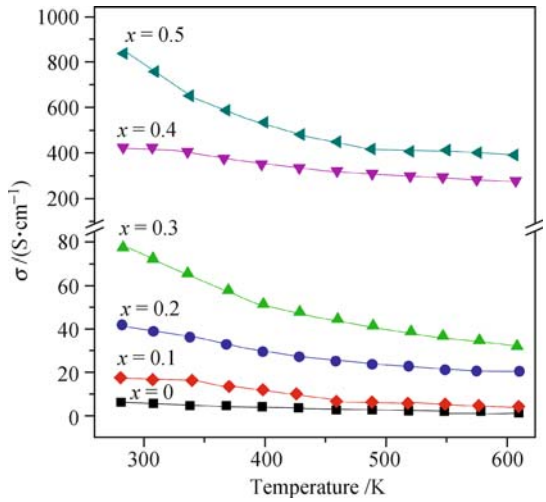

Fig. 26 Temperature dependences of the electrical conductivity of $Cu_{1+x}In_{1-x}Se_2$ ($x = 0$–0.5) samples.

From the above results, it is clear that as the value of x increases, the electrical conductivity can be dramatically increased either at room temperature or at higher temperature. Furthermore, the electrical conductivities decrease with increasing temperature for all the samples, showing typical metal conducting behavior. This means that Cu_{In} in $Cu_{1+x}In_{1-x}Se_2$ samples is a kind of shallow acceptor ionized completely at room temperature [43].

Figure 27 displays the temperature dependence of Seebeck coefficient of $Cu_{1+x}In_{1-x}Se_2$ in the range from room temperature to 625 K. As the copper substitution concentration x increases, the Seebeck coefficient decreases slightly. This might be caused by the gradually increasing carrier density of the samples with the increase of Cu-doping concentration. The Seebeck coefficient of the samples increased with increasing temperature over the entire temperature range. At room temperature, the values of Seebeck coefficient for $Cu_{1+x}In_{1-x}Se_2$ ($x = 0$–0.5) are relatively low, about 5–15 μV/K. However, as the temperature increases, the values increase evidently for all the samples. The Seebeck coefficients are 80 μV/K for $CuInSe_2$, around 65 μV/K for $Cu_{1.4}In_{0.6}Se_2$, and 57 μV/K for $Cu_{1.5}In_{0.5}Se_2$ at 625 K, respectively.

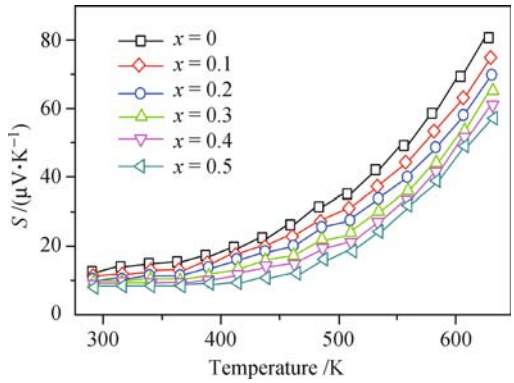

Fig. 27 Temperature dependences of the Seebeck coefficient of $Cu_{1+x}In_{1-x}Se_2$ ($x = 0$–0.5) samples.

As a consequence, in the $Cu_{1+x}In_{1-x}Se_2$ system, the optical band gap reduces gradually, the electrical conductivity increases dramatically and the Seebeck coefficient decreases slightly with increasing Cu-doping concentration. It is likely that lattice distortions and additional holes introduced by Cu doping are attributed to the improved conductivity and the decreased band gap and Seebeck coefficient.

The photovoltaic (PV) behavior of heterojunction thin film solar cells based $CuInSe_2$ depends significantly on its microstructural characteristics. Hence, synthesis kinetics and grain growth of polycrystal $CuInSe_2$ are significant properties. In the following work, $CuInSe_2$ ingots have been prepared by direct reaction of Cu_2Se/In_2Se_3 in evacuated quartz ampoule. The aim of this work is to study the temperature dependence of the microstructure of $CuInSe_2$ material along with the electrical properties.

The temperature dependences of the microstructure are shown in the SEM micrographs of $CuInSe_2$ samples prepared at (a) 600°C, and (b) 700°C for different sintering time (see in Fig. 28). At 600°C, the grain sizes of the samples were 5–10 μm below 1 h and did not grow much bigger after long time sintering. The impurity phases in XRD patterns can also be found in SEM micrographs, shown as small light particles marked in the micrographs only below 1 h. These may indicate that 600°C provides just enough driving force to Cu_2Se/In_2Se_3 reaction, making grain growth insensitive to sintering time. However, at 700°C, the grain sizes grew very fast with the sintering time. A clear grain growth path was shown in the micrographs and the size became as big as 15–20 μm in 3 h.

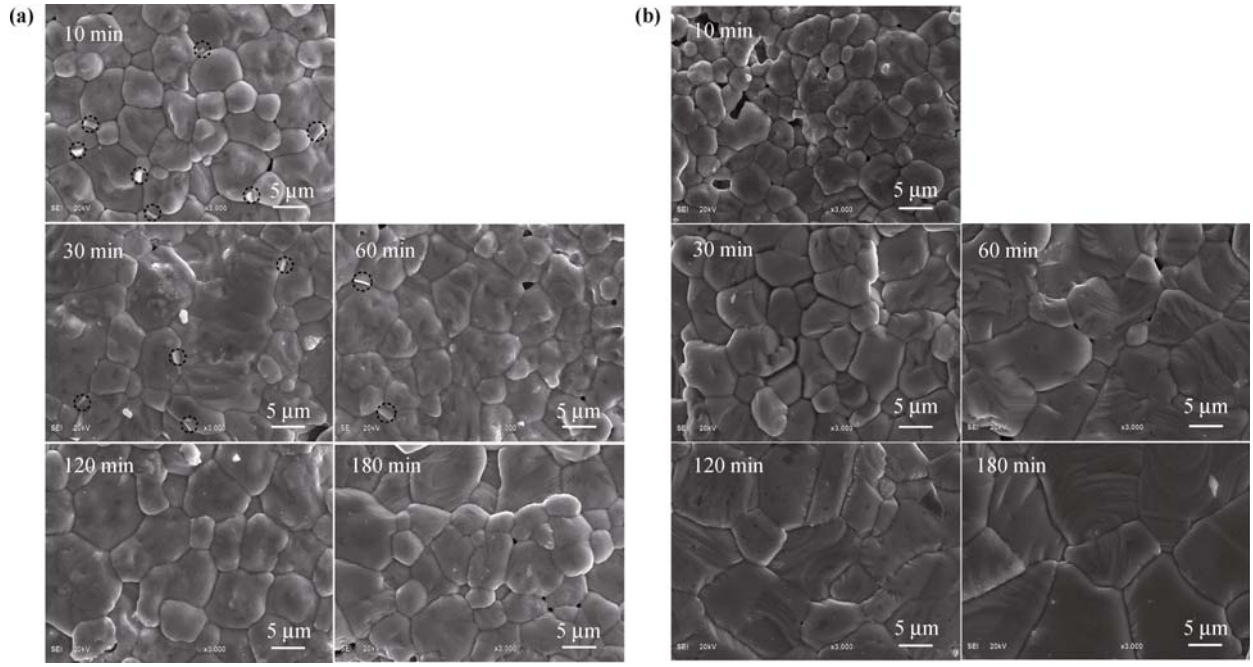

Fig. 28 SEM micrographs of $CuInSe_2$ samples prepared at **(a)** 600°C and **(b)** 700°C.

Figure 29 depicts the plot of $(\alpha h\nu)^2$ against $h\nu$ of $CuInSe_2$ samples prepared at (a) 600°C, and (b) 700°C for different sintering time, from which the directly allowed band gap can be estimated. The optical band gaps were found shifting from 0.83 eV to 0.86 eV at 600°C and 0.85 eV to 0.89 eV with the sintering time rising. This kind of sight shift may have a lot to do with the grain size effect of the samples. Figure 30 shows the temperature dependence of the resistivity of $CuInSe_2$ samples prepared at (a) 600°C, and (b) 700°C for different sintering time. At 600°C, according to the XRD patterns and the SEM micrographs, impurity phases and imperfections of the samples disappeared as the sintering time

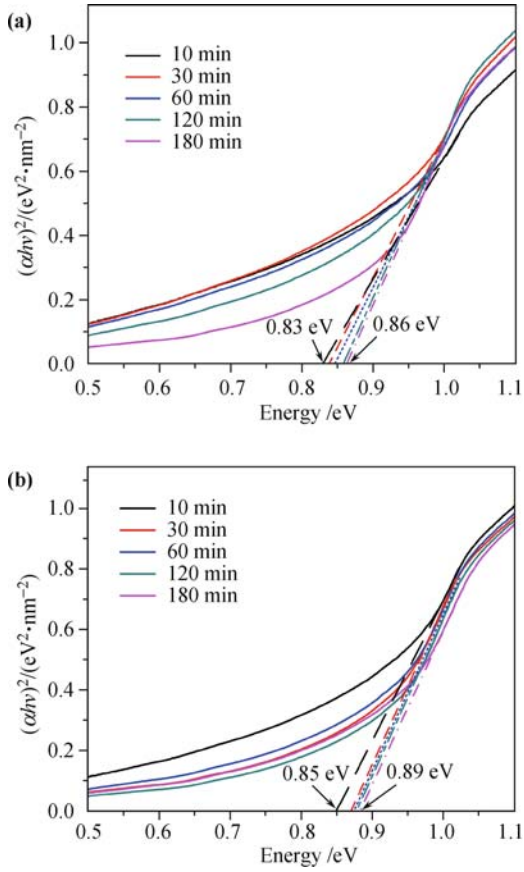

Fig. 29 The plots of $(\alpha h\nu)^2$ versus photo energy for $CuInSe_2$ samples prepared at **(a)** 600°C and **(b)** 700°C.

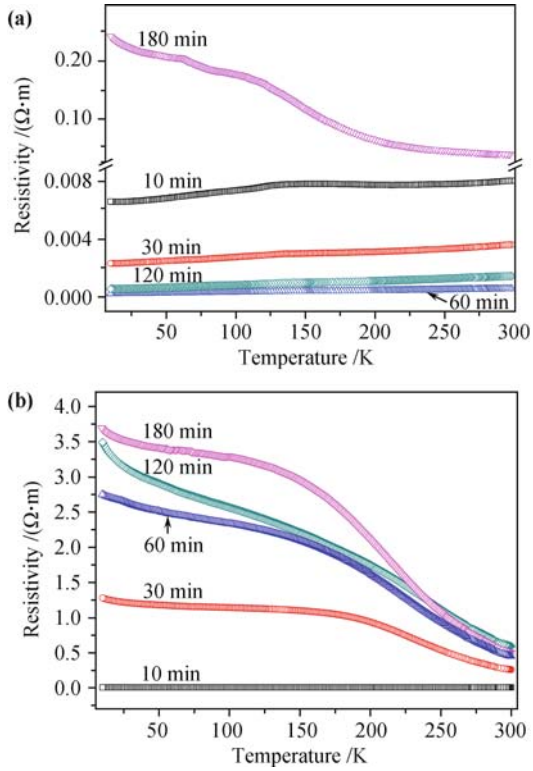

Fig. 30 Temperature dependence of the resistivity of $CuInSe_2$ samples prepared at **(a)** 600°C and **(b)** 700°C.

prolonged. Thus, the resistivity of $CuInSe_2$ samples was dropping with them. However, at 700°C and after 1 h at 600°C, the resistivity of $CuInSe_2$ samples increased with the sintering time prolonged. Since grain boundary makes a significant contribution to electroconductibility of $CuInSe_2$, the grain growth reduces the grain boundary, cuts the conducting path and increases the resistivity.

2.7 Fundamental researches of Cu_2MSnQ_4 (M = Zn, Cd; Q = S, Se) for new absorber layer

A potential long-term issue with CIGS technology is the available resource of indium. Hence, a quaternary chalcogenide compound–copper zinc tin sulphide (CZTS) is considered as the next generation in free absorber material, which might be the ideal substitute for CIGS. Actually, a big material family of Cu_2MSnQ_4 (M = Zn, Cd and more transition metal; Q = S, Se) have the potential to become photovoltaic materials. However, these compounds are far from being fully understood. The fundamental researches of their electrical transport and optical properties are necessary and have provided many unique results.

Recent researches about the electrical transport properties of Cu_2MSnQ_4 (M = Zn, Cd; Q = S, Se) show the highly controllable conductivities and great thermoelectric performances [44–46]. The temperature spectra of σ for Cu_2ZnSnQ_4 and $Cu_{2.1}Zn_{0.9}SnQ_4$ (Q = S, Se) in Fig. 31(a) show a large increase from sulfide to selenide. For both, Cu doping results in a dramatic increase of σ reaching 2600 $S{\cdot}m^{-1}$ for $Cu_{2.1}Zn_{0.9}SnS_4$ and 86 000 $S{\cdot}m^{-1}$ for $Cu_{2.1}Zn_{0.9}SnSe_4$, which may be attributed to creation of holes (Cu^{2+} $3d^9$ vs. Cu^{+} $3d^{10}$) and conversion of insulating paths ($[ZnQ_4]$) to conducting paths ($[CuQ_4]$). Although Cu_2ZnSnS_4 is a normal semiconductor exhibiting a thermally activated behavior for σ, the strong thermal activation is largely removed by Cu-doping. Selenide samples show a metallic behavior in analogy to the reported trend for $LaCuOQ$ (Q = S, Se, Te): the sulfide and selenide are semiconductive, and the telluride is metallic [47]. A flat $\sigma(T)$ has also been observed in LnCuOTe (Ln = La, Ce, Nd) [47] and is indicative of the metallic behavior with a relatively short mean free path limited by defect/impurity scattering rather than phonon scattering. These features are all consistent with the interpretation that hole conductivity comes from the hybridization of Cu 3d with Q np (Q np = S 3p, Se 4p, Te 5p) near the VBM [47].

Hole conduction was verified by both positive Seebeck coefficients [Fig. 31(b)]. The Seebeck coefficients slightly increase with the temperature. These values are comparable to those of the well-known binary TE materials. Notably, both S and σ increase with the temperature in Cu_2ZnSnS_4, which was confirmed using duplicate samples and different measuring instruments (data not shown). The enhanced σ in doped $Cu_{2.1}Zn_{0.9}SnQ_4$ and the mostly positive temperature dependence of S and σ cause the power factors ($PF = S^2\sigma$) to increase especially at higher temperatures, reaching 0.58 $mW{\cdot}m^{-1}{\cdot}K^{-2}$ and 1.01 $mW{\cdot}m^{-1}{\cdot}K^{-2}$ at 700 K for $Cu_{2.1}Zn_{0.9}SnS_4$ and $Cu_{2.1}Zn_{0.9}SnSe_4$, respectively.

Figure 32 shows the temperature dependence of ther-

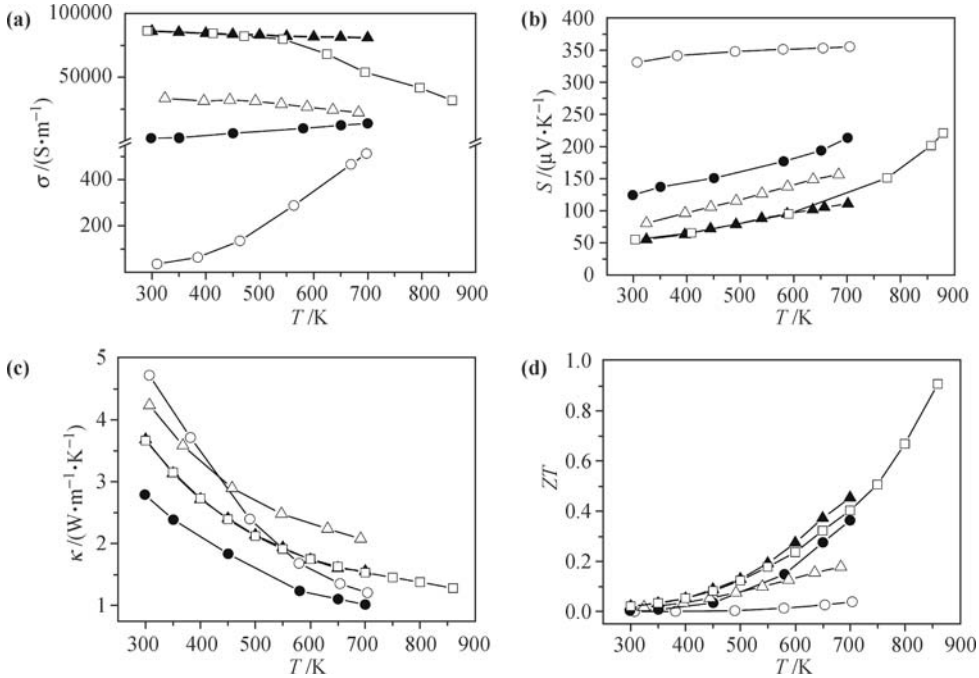

Fig. 31 Temperature dependence of electrical conductivity **(a)**, Seebeck coefficient **(b)**, total thermal conductivity **(c)** and figure of merit ZT **(d)** for Cu_2ZnSnS_4 (○), $Cu_{2.1}Zn_{0.9}SnS_4$ (●), $Cu_2ZnSnSe_4$ (△), $Cu_{2.1}Zn_{0.9}SnSe_4$ (▲), and sodium silicate coated $Cu_{2.1}Zn_{0.9}SnSe_4$ (□) during first heating cycle. Note in (c) the symbols ▲ and □ nearly coincide from 300 K to 700 K. Reproduced from Ref. [45], Copyright © 2009 The American Institute of Physics.

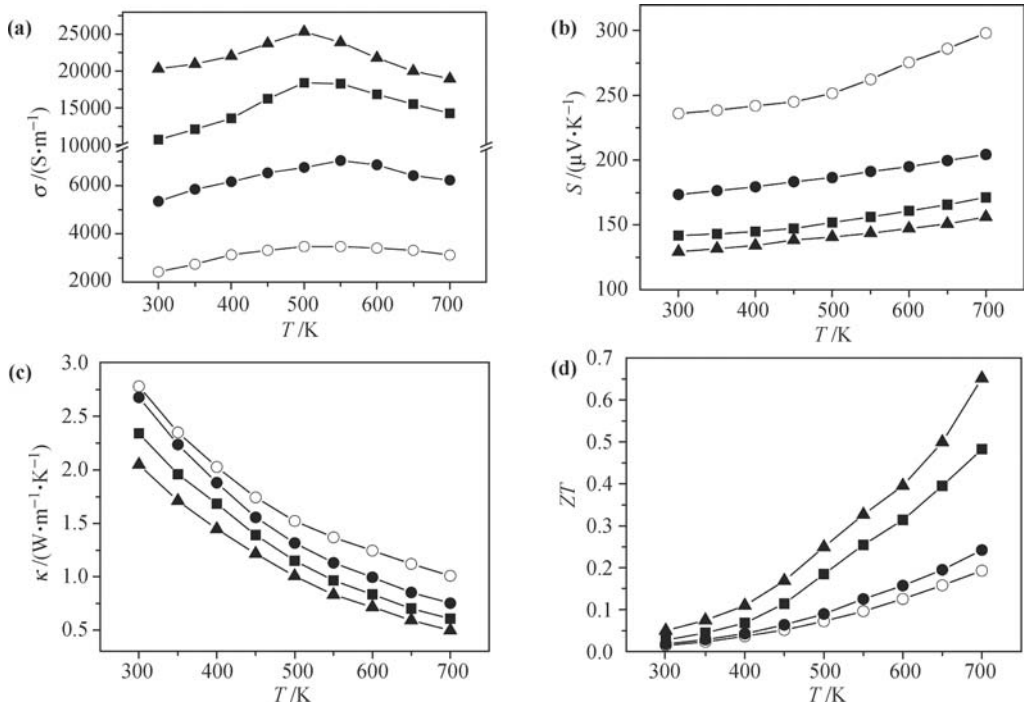

Fig. 32 Temperature dependence of electrical conductivity **(a)**, Seebeck coefficient **(b)**, total thermal conductivity **(c)** and figure of merit ZT **(d)** for $Cu_{2+x}Cd_{1-x}SnSe_4$ with $x = 0$ (○), $x = 0.025$ (●), $x = 0.05$ (■) and $x = 0.10$ (▲). Reproduced from Ref. [44], Copyright © 2009 The Wiley Interscience.

moelectric properties for $Cu_{2+x}Cd_{1-x}SnSe_4$ (x = 0, 0.025, 0.05, 0.10). As shown in Fig. 32(a), σ increases to some degree and then inversely decreases with the increasing temperature. Remarkably, Cu doping results in a dramatic increase of σ for Cu_2MSnQ_4 (M = Zn, Cd; Q = S, Se), reaching 20 308 $S{\cdot}m^{-1}$ at room temperature for $Cu_{2.10}Cd_{0.90}SnSe_4$, which is about 6-fold higher than that of $Cu_2CdSnSe_4$ (3131 $S{\cdot}m^{-1}$). It may be attributed to the creation of holes (Cu^{2+} $3d^9$ vs. Cu^+ $3d^{10}$) and conversion of electrically insulating paths ($[MSnQ_4]$) to electrically conducting paths ($[Cu_2Q_4]$). This feature is consistent with the interpretation that hole conductivity comes from the hybridization of Cu 3d with Q np (Q np = S 3p, Se 4p, Te 5p) near the VBM in LaCuOQ (Q = S, Se, Te) [48].

As expected from a simple electron count, all the samples present hole conduction, which were verified by the positive Seebeck coefficients shown in Fig. 32(b). They rise steadily in nearly a straight line as temperature increases for $Cu_{2+x}Cd_{1-x}SnSe_4$ (x = 0, 0.025, 0.05, 0.10). At 700 K, $Cu_2CdSnSe_4$ suffers a high S of 298 $\mu V{\cdot}K^{-1}$, higher than that of some well-known thermoelectric materials, which may be attributed to the wide band gap. Opposite to σ, partial substitution of Cu for Cd leadsto a lower S. It is common in many other thermoelectric materials due to the increasing carrier concentration from doping. Due to the highly enhanced σ of doped $Cu_2CdSnSe_4$, the power factors (PF = $S^2\sigma$) is greatly improved, which varies similarly to σ according to the dependence of temperature. However, the power factor met the maximum value at 500 K, about 5.1 $\mu W{\cdot}cm^{-1}{\cdot}K^{-2}$ for $Cu_{2.10}Cd_{0.90}SnSe_4$, which is comparable to the Zintl compound $BaZn_2Sb_2$ [49] at 675 K and only one half of optimized Bi_2Te_3 alloy at room temperature [50].

Figures 33(a) and (b) display the temperature dependence of electrical conductivity σ and Seebeck coefficient S for $Cu_2ZnSn_{1-x}In_xSe_4$ (x = 0, 0.05, 0.10, and 0.15). The matrix $Cu_2ZnSnSe_4$ shows p-type conduction with relatively low electrical conductivity and high Seebeck coefficient over the whole temperature range. The electrical conductivity increases significantly with increasing x, from 4500 Sm^{-1} ($Cu_2ZnSnSe_4$) to 29 000 $S{\cdot}m^{-1}$ ($Cu_2ZnSn_{0.85}In_{0.15}Se_4$), while the Seebeck coefficient decreases from 130 $\mu V{\cdot}K^{-1}$ ($Cu_2ZnSnSe_4$) to 75 $\mu V{\cdot}K^{-1}$ ($Cu_2ZnSn_{0.85}In_{0.15}Se_4$), which results in the enhancement of power factor ($S^2\sigma$). This is consistent with the change of hole concentration that was measured as 1 × 10^{19} cm^{-3} for $Cu_2ZnSnSe_4$ and 6 × 10^{20} cm^{-3} for $Cu_2ZnSn_{0.85}In_{0.15}Se_4$.

3 Summary and outlook

Herein, the basic band diagram and working principle of a typical thin-film semiconductor solar cell are addressed, and some recent developments of solar materials and technologies for chalcogenide thin film photovoltaic cells are reviewed. These new fabrications and new solar materials can improve photovoltaic efficiency and reduce manufacturing cost, including Mo thin films deposited by

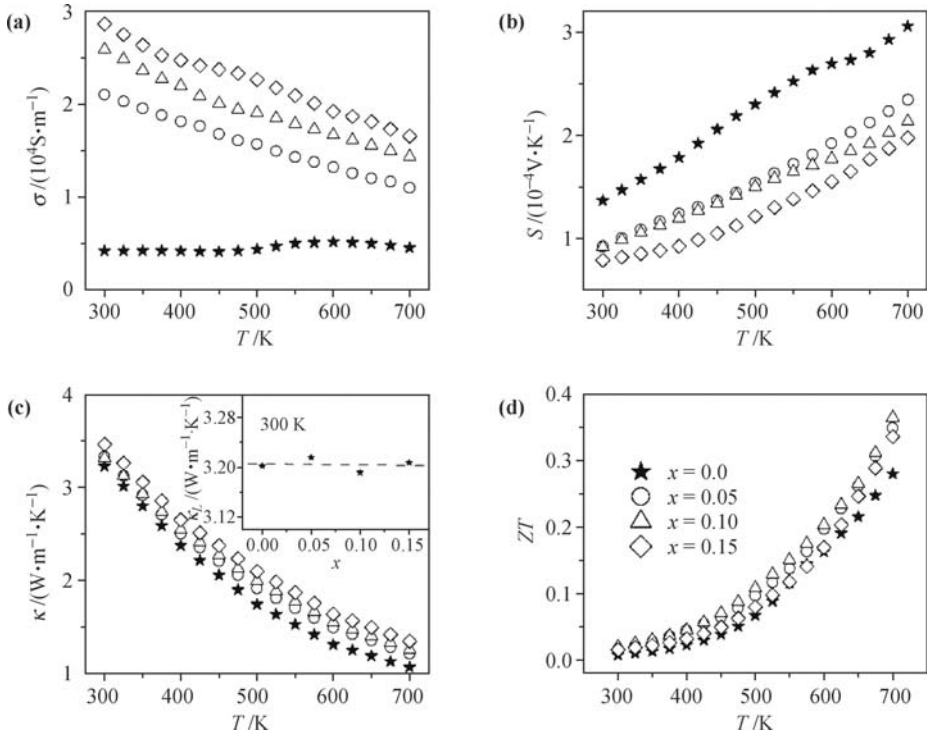

Fig. 33 Temperature dependence of electrical conductivity **(a)**, Seebeck coefficient **(b)**, thermal conductivity (insert is the lattice thermal conductivity at 300 K) **(c)**, and dimensionless figure of merit ZT **(d)** for $Cu_2ZnSn_{1-x}In_xSe_4$. Reproduced from Ref. [46], Copyright © 2009 The American Institute of Physics.

RF sputtering as back contact of CIGS cells, highly surface-textured ZnO:Al films sputtered by a new two-step method as front contact of CIGS cells, boron-doped graphene prepared by a rapid method as back contact of CdTe cells, nanostructured ZnO/SiO_2 fabricated by sol-gel methods as broadband antireflection coatings of solar cells, $Cd_{1-x}Zn_xS$ thin films as a wider-band-gap buffer layer of CIGS cells. Fundamental studies of the classic ($CuInSe_2$) and new (Cu_2MSnQ_4: M = Zn, Cd; Q = S, Se) absorber layers for CIGS cells are also discussed.

Thin film solar cell is one of the most practical solutions for our energy source in future. CdTe cells and CIGS cells are promising technologies, giving opportunities to these potentially lower cost approaches for application. All the efforts need to be focused on improving the efficiency and lowering the cost of chalcogenide solar cells. To achieve these goals, many kinds of advanced solar materials and new fabrication methods should be developed with a focus on high-performance and low-cost parts for the thin-film solar cells to improve light trapping and antireflection, quantum efficiency and collection of photo-generated carrier. As new high-performance solar materials, economic and abundant available materials (e.g., Cu_2ZnSnS_4 as photovoltaic absorber, graphene as front contact, etc.) need to be developed into commercial cells. Novel wide-band solar-spectrum absorber materials (either gradient-band-gap materials or intermediate band materials) are also one of the directions for next generation high-efficiency and low-cost solar cells. The new development of key supporting materials such as n-type transparent conducting films, novel p-type transparent conducting films, anti-reflection coatings, high temperature durable flexible substrates, and so on, are in high demand. It is foreseeable that much more efforts will be focused on the development of these new materials and will push the mature thin film solar cells technologies into the photovoltaics market.

Acknowledgements This work was financially supported by the National Basic Research Program of China (973 Program) (Grant Nos. 2007CB936704 and 2009CB939903), the National Natural Science Foundation of China (Grant Nos. 50902143 and 50821004), and the Science and Technology Commission of Shanghai (Grant Nos. 0752nm016 and 0952nm06500). The authors thank Dr. Yaoming Wang, Dr. De-zeng Li, Dr. Hui Bi, and Mr. Tian-quan Lin for their helpful suggestions.

References

1. M. A. Green, J. Mater. Sci. Mater. Electron., 2007, 18(S1): S15
2. J. M. Woodcock, H. Schade, H. Maurus, B. Dimmler, J. Springer, and A. Ri-caud, in: Proc. 14th Europ. Photovolt. Solar Energy Conf., edited by H. A. Ossenbrink, P. Helm, and H. Ehmann, Bedford, UK: Stephans, 1997: 857
3. J. G. Mutitu, S. Y. Shi, C. H. Chen, T. Creazzo, A. Barnett, C. Honsberg, and D. W. Prather, Opt. Express, 2008, 16(19): 15238
4. C. G. Granqvist, Thin Solid Films, 1990, 193–194: 730
5. D. S. Ginley and C. Bright (Eds.), MRS Bull., 2000, 25: 15
6. H. Kim, J. S. Horwitz, G. P. Kushto, Z. H. Kafafi, and D. B. Chrisey, Appl. Phys. Lett., 2001, 79(3): 284

7. D. Wan, F. Huang, Y. Wang, X. Mou, and F. Xu, ACS Appl. Mater. Interfaces, 2010, 2(7): 2147
8. R. F. Xiao, J. I. D. Alexander, and F. Rosenberger, Phys. Rev. A, 1991, 43(6): 2977
9. I. Volintiru, M. Creatore, B. J. Kniknie, C. I. M. A. Spee, and M. C. M. van de Sanden, J. Appl. Phys., 2007, 102(4): 043709–1
10. K. Sato, Y. Gotoh, Y. Wakayama, Y. Hayashi, K. Adachi, and H. Nishimura, Rep. Res. Lab. Asahi Glass Co. Ltd., 1992, 42: 129
11. W. N. Shafarman and J. E. Phillips, Proceedings of the 25th IEEE Photovolt, D. C. Washington: Spec. Conf. IEEE, 1996: 917
12. V. G. Glebovsky and E. A. Markaryans, J. Alloys Comp., 1993, 190(2): 157
13. Y. G. Shen, Mater. Sci. Eng. A, 2003, 359(1–2): 158
14. T. J. Vink, M. A. J. Somers, J. L. C. Daams, and A. G. Dirks, J. Appl. Phys., 1991, 70(8): 4301
15. A. K. Geim and K. S. Novoselov, Nat. Mater., 2007, 6(3): 183
16. T. Q. Lin, F. Q. Huang, J. Liang, and Y. X. Wang, Energy & Environ. Sci., DOI: 10.1039/c0ee00512f
17. Z. S. Wu, S. F. Pei, W. C. Ren, D. M. Tang, L. B. Gao, B. L. Liu, F. Li, C. Liu, and H. M. Cheng, Adv. Mater., 2009, 21(17): 1756
18. K. S. Krishnan and N. Ganguli, Nature, 1939, 144(3650): 667
19. A. Luque and S. Hegedus, Handbook of Photovoltaic Science and Engineering, New York: Wiley, 2003
20. R. B. Petit and C. J. Brinker, Sol. Energy Mater., 1986, 14: 269
21. C. Brückner, B. Pradarutti, O. Stenzel, R. Steinkopf, S. Riehemann, G. Notni, and A. Tünnermann, Opt. Express, 2007, 15(3): 779
22. S. A. Boden and D. M. Bagnall, Appl. Phys. Lett., 2008, 93(13): 133108
23. Z. Chen and L. Gao, J. Cryst. Growth, 2006, 293(2): 522
24. M. K. Kim, D. K. Yi, and U. Paik, Langmuir, 2010, 26(10): 7552
25. C. J. Brinker and G. W. Scherer, Sol–Gel Science, San Diego: Academic Press, 1990
26. A. Pudov, J. Sites, and T. Nakada, Jpn. J. Appl. Phys., 2002, 41(Part 2, No. 6B): L672
27. Z. Zhen, Z. Kui, and H. Fuqiang, J. Inorg. Mater., 2010, 25: 1
28. H. Fujiwara, Spectroscopic Ellipsometry Principles and Applications, England: John Wiley & Sons Ltd., 2007
29. D. Lincot and R. O. Borges, J. Electrochem. Soc., 1992, 139(7): 1880
30. F. Gode, C. Gumus, and M. Zor, J. Cryst. Growth, 2007, 299(1): 136
31. G. Conibeer, M. Green, R. Corkish, Y. Cho, E. C. Cho, C. W. Jiang, T. Fangsuwannarak, E. Pink, Y. Huang, T. Puzzer, T. Trupke, B. Richards, A. Shalav, and K. Lin, Thin Solid Films, 2006, 511: 654
32. T. Terasako, Y. Uno, T. Kariya, and S. Shirakata, Sol. Energy Mater. Sol. Cells, 2006, 90(3): 262
33. N. Stratieva, E. Tzvetkova, M. Ganchev, K. Kochev, and I. Tomov, Sol. Energy Mater. Sol. Cells, 1997, 45(1): 87
34. A. Rothwarf and K. W. Böer, JPSSC 10(2-B), Progress in Solid-State Chemistry, 1975, 10(part 2): 71
35. J. H. Schon, V. Alberts, and E. Bucher, Thin Solid Films, 1997, 301(1–2): 115
36. S. B. Moorthy, R. Dhanasekaram, and P. Ramasamy, Thin Solid Films, 1991, 198: 209
37. E. Tzvetkova, N. Stratieva, M. Ganchev, I. Tomov, K. Ivanova, and K. Kochev, Thin Solid Films, 1997, 311(1–2): 101
38. A. Zouaoui, M. Lachab, M. L. Hidalgo, A. Chaffa, C. Llinares, and N. Kesri, Thin Solid Films, 1999, 339(1–2): 10
39. W. Henkel, H. D. Hochheimer, C. Carlone, A. Werner, S. Ves, and H. G. Von Schnering, Phys. Rev. B, 1982, 26(6): 3211
40. M. Hanias, A. N. Anagnoustopoulos, K. Kambas, and J. Spyridelis, Physica B, 1989, 160(2): 154
41. J. F. Guillemoles, Thin Solid Films, 2000, 361–362(1–2): 338
42. A. Zunger, Thin Solid Films, 2007, 515(15): 6160
43. J. Yao, C. N. Kline, H. Gu, M. Yan, and J. A. Aitken, J. Solid State Chem., 2009, 182(9): 2579
44. M. L. Liu, I. W. Chen, F. Q. Huang, and L. D. Chen, Adv. Mater., 2009, 21(37): 3808
45. M. L. Liu, F. Q. Huang, L. D. Chen, and I. W. Chen, Appl. Phys. Lett., 2009, 94(20): 202103
46. X. Y. Shi, F. Q. Huang, M. L. Liu, and L. D. Chen, Appl. Phys. Lett., 2009, 94(12): 122103
47. M. L. Liu, L. B. Wu, F. Q. Huang, L. D. Chen, and J. A. Ibers, J. Solid State Chem., 2007, 180(1): 62
48. S. R. Hall, J. T. Szymański, and J. M. Stewart, Can. Mineral., 1978, 16: 131
49. X. J. wang, M. B. Tang, J. T. Zhao, H. H. Chen, and X. X. Yang, Appl. Phys. Lett., 2007, 90: 232107
50. G. S. Nolas, J. Sharp, and H. J. Goldsmid, Thermoelectrics: Basic Principles and New Materials Developments, New York: Springer, 2001, Chap. 5